INTRAVITAL IMAGING OF MELANOMA IN COMBINATION WITH MOLECULAR ANALYSIS REVEALS KEY CHANGES IN STROMAL ECM AND TUMOR BEHAVIOR IN PERSISTENCE AGAINST MEKi

Hailey Elizabeth Brighton

A dissertation submitted to the faculty at the University of North Carolina at Chapel Hill in partial fulfillment of the requirements for the degree of Doctorate of Philosophy in the Department of Cell Biology and Physiology in the School of Medicine.

Chapel Hill
2017

Approved By:

James E. Bear

Norman E. Sharpless

William Y. Kim

Keith Burridge

Andrew C. Dudley

ABSTRACT

Hailey Elizabeth Brighton: Intravital imaging of melanoma in combination with molecular analysis reveals key changes in stromal ECM and tumor behavior in persistence against MEKi
(Under the direction of James E. Bear)

Melanoma is a devastating disease, and while a number of targeted therapies are used to treat patients with malignant melanoma, tumors become resistant. Understanding tumor response to targeted therapies and how therapeutic strategies fail is a critical challenge in modern oncology. To investigate tumor behavior and response to a selective small molecule inhibitor of MEK1/2 (Trametinib) *in vivo*, we developed an intravital imaging approach to directly visualize drug response in a $BRAF^{V600E}$/PTEN-null mouse model of melanoma by genetically incorporating a tdTomato fluorescent reporter allele ($tdTomato^{LSL}$). Through highly localized application of tamoxifen (4-HT) and noninvasive, serial intravital microscopy, I was able to directly visualize formation and progression of tumors at the single cell level *in situ* longitudinally over time. I directly imaged primary tumors in mice throughout treatment with MEKi and observed changes in tumor cell behavior during drug response for twelve weeks. I identified a clear relationship between bundled collagen and tumor cell survival in response to MEKi and collaborated with the Johnson lab to couple this model with transcriptome and kinome reprogramming analysis. Molecular analysis of tumors at early and late stages on MEKi identified a phenotypic shift toward an epithelial phenotype, characterized by c-Kit activity and the induction of a EMT_down and PI3K/AKT survival pathway signatures for melanoma persistence in vivo. Together, these approaches give a holistic view of the complex changes of tumor cells and stromal tissue in response to targeted therapy and provide insight for future treatment strategies.

For my friends and family. My success is because of you.

ACKNOWLEDGEMENTS

Because of the dynamic and transitory nature of a laboratory, no student experiences one lab the same. I have been extremely fortunate during my time in the Bear lab, working with not only some of the best scientists, but also some of the best people at UNC. Each member has influenced me and my graduate work in remarkable ways. I would like to thank Emma Wu, who taught me how to passage cells without contamination, and Liz Haynes, who was my cheerleader throughout. I am filled with gratitude for Keefe Chan, who exhibited robotic-like patience in every question I asked (there were many), introduced me to intravital imaging, and who became one of my greatest mentors in so many ways. I would like to extend extra special thanks to Seth Zimmerman and Jeremy Rotty, who have been my two constants, always willing to humor me in discussing my crazy ideas, and who made impossible days worthwhile. Thanks to Alicia Tagliatela, who now carries the torch with a smile. And, finally, I would like to thank Jim Bear, without whom, this project and my success would not exist. Jim taught me to be driven by scientific curiosity and always pushed me to fearlessly pursue questions and develop opportunities, even when I struggled with the unknown.

Someone once told me that the key to success is to never be the smartest person in the room, and my friends and family ensure that I am very successful. I am incredibly grateful for you. Special thanks to all of my parents, my brother and sister-in-law, and my best friend and tortuga, Kayla. Thanks to Diana for laughs, and to Kyle for playing pool with me every week, even though I only won a few times. And I would like to thank all of the creatures that helped make this work possible. Thanks to the mice who participated, to the Mouse Phase I Unit for creating them, and thanks to DLAM for keeping them well hydrated and monitored.

TABLE OF CONTENTS

LIST OF FIGURES

LIST OF TABLES

LIST OF ABBREVIATIONS AND SYMBOLS

CAF – Cancer associated fibroblast

CI – Confidence interval

CL – Collagen

Dpa – days post-4-HT application

ECM – Extracellular matrix

EMT – Epithelial to mesenchymal transition

GEM – Genetically Engineered Mouse

H&E – Hematoxylin and Eosin staining

4-HT – 4-Hydroxytamoxifen

IR - Infrared

LOX – Lysyl oxidase

MAPK – Mitogen activated protein kinase

MET – Mesenchymal to epithelial transition

MIB/MS - multiplexed-inhibitor bead affinity chromatography coupled with mass spectrometry

MT – Masson's trichrome staining

PBT –*Tyr::CreER; BRAF^{CA};PTEN$^{lox/lox}$* GEM model

RTK – Receptor Tyrosine Kinase

SHG – Second Harmonic Generation

TAM – Tumor associated macrophage

UV – Ultraviolet

λ – Wavelength

wpa – Weeks pos-4-HTt-application

CHAPTER 1: INTRODUCTION

1.1 Introduction and a brief description of melanoma

Melanoma is the most dangerous form of skin cancer, which arises when a melanocyte within the dermis aberrantly proliferates, generating a tumor cell mass. Melanocytes are dendritic cells within the dermis and epidermis that secrete melanin-containing melanosomes to keratinocytes in the epidermis to protect them from UV-mediated DNA damage. UV irradiation is the main carcinogen associated with melanoma development, as it causes T-T dimers within DNA, which can induce genetic mutations that lead to aberrant cell survival and growth [1]. Melanocytes can protect the skin from UV damage through melanosome secretion. However, a balance must exist between melanin production and sunlight exposure, as ultraviolet B is required for vitamin D synthesis, which is necessary for proper bone development [2].

Similar to other types of cancers, melanoma is typically a disease of the elderly. However, the incidence of melanoma is steadily rising due to both an increase in detection methods and changes in behavioral trends, such as “tanning”, which has become culturally popularized over the past several decades. To drive aberrant growth within a single melanocyte, genetic mutations within both an oncogene and a tumor suppressor gene must occur to deregulate cellular signaling and cause a melanocyte to divide unchecked. Fortunately, in most cases, constitutive activation of pro-proliferative oncogenes (e.g. BRAF, NRAS, KIT, PI3K) will initiate oncogene induced senescence (OIS), which is a protective mechanism to inhibit tumor formation. In the case of most nevi formation, activation of this pathway will result in a round mole or an age spot [3]. Additionally, while UV irradiation is the largest risk factor in developing melanoma, hereditary genetic variance can also predispose and increase one’s risk of

developing this disease, similar to other cancers. Common pathways associated with increased risk that can drive malignant progression are described below and are depicted in Figure 1.1.

While melanoma only accounts for approximately 2% of all skin cancers, it is by far the most aggressive [4]. Melanoma cells are particularly perilous in clinical settings because they are highly migratory, invasive, and they can metastasize very quickly to distant target organs including lymph nodes, lung, liver, and brain (Fig. 1.2). Once this cancer has metastasized, a patient has only approximately a 15% chance of surviving within the next 5 years. While new treatment strategies for malignant melanoma have been on the rise and may increase a patient's life expectancy, tumors almost always regrow and become resistant to the therapy, which inevitably fails.

1.2 Commonly deregulated pathways that promote melanoma growth

The most commonly mutated oncogene in malignant melanoma is BRAF, a key player in the MAPK signaling pathway, promoting cell growth and division when activated (Fig. 1.1). Mutations in this gene are detected in greater than 50% of human melanomas, with BRAFV600E being the most commonly identified mutation in the clinic [5]. When this mutation (BRAFV600E) occurs, the kinase's activation loop (residues 596-600) does not bind to inhibit the P-loop (residues 464-471), which associates with the phosphate group in ATP for BRAF kinase activity [6]. Therefore, this mutation enables constitutive activity of BRAF and promotes activation of MEK, which is directly downstream in the MAPK pathway.

In addition to gain of function in the BRAF oncogene, a loss of function mutation in a tumor suppressor gene, which can signal the cell to stop dividing, must also occur to form a tumor. The phosphatase PTEN is the second most commonly mutated tumor suppressor in cancers, second only to p53, and PTEN loss has been shown to cooperate with BRAFV600E to form melanoma [7,8]. Loss of PTEN causes deregulation of the PI3-Kinase and AKT signaling pathways, which will deregulate cell checkpoint mechanisms, promoting cell growth and avoiding apoptosis. Mapping the signaling pathways that promote survival has defined specific

kinases for therapeutic targeting. However, understanding the functional biology of melanoma development at the cell level is also important for identifying tumor behaviors that can be targeted with new therapies.

1.3 Mechanisms of invasion & metastasis

Melanoma is the most dangerous form of skin cancer because it quickly metastasizes (Figure 1.2). Traditionally, metastasis is known to occur through both lymphatic and hematogenous spread. Melanoma cell dissemination via the lymphatics is the most common, can occur at very early stages (between stage I and II), and results in tumor cell seeding within regional lymph nodes. Hematogenous metastasis occurs when tumor cells invade into and migrate through the vasculature to later form colonies in target organs, such as the liver, lungs, bone, and brain [9]. This typically occurs in tumors at later stages (stage III or IV), and is a strong indicator of poor prognosis. Interestingly, it is now believed that melanoma cells may also migrate through a variety of other mechanisms to achieve metastasis. For instance, tumor cells may migrate along nerve fiber tracks, use vascular mimicry to invade and migrate along endothelial cells, degrade or reorganize extracellular matrix to promote migration and invasion away from the original tumor mass, or recruit a variety of stromal cells and factors to enhance their metastatic capacity [10,11].

Previously, it was widely held that the process of invasion and metastasis occurred via migration of single cells. However, now many studies are now revealing that metastasis may involve, or in fact require, collective migration of multiple cancer cells from the primary tumor [12,13]. Work in the cancer stem cell field has shown that cancer stem cells can attach themselves to more pro-migratory tumor cells, which do most of the heavy lifting in the metastatic cascade. In this model, migratory tumor cells invade through the endothelial barrier to transport both itself and the attached cancer stem cell through the blood stream and extravasate into distant tissue. It is thought that here, the tumor stem cells, which are pro-proliferative, are then responsible for the development of micrometastases and colonization of target organs to form secondary and

tertiary tumors. As outlined in Table 1.2 and discussed below in further detail, there are limited mouse models of melanoma that can properly recapitulate the individual stages of tumor development that lead to the metastatic cascade in vivo. For this reason, among several others, it remains unknown whether existing therapeutics promote, inhibit, or have no effect on tumor cell invasion and dissemination. We hope to use the melanoma model system that I have developed in my graduate career to mimic and interrogate metastasis as it occurs in clinical settings, which will be discussed in further detail in Chapter 3.

1.4 Treatment strategies and issues

Since cancer is such a dynamic and heterogeneous living tissue, there are a great number of challenges in successfully treating this disease. While a melanoma is primarily composed of quickly proliferating melanoma cells, the tumor stroma can also promote malignancy and resistance to therapeutics. A variety of cell types and factors influence the tumor microenvironment [14]. Infiltrating immune cells such as tumor associated macrophages (TAMs); cancer associated fibroblasts (CAFs), which can remodel the ECM; endothelial cells that make up the leaky tumor vasculature; hair follicles that provide a stem cell niche; nerve fibers; lymphatic vessels that can promote tumor cell dissemination; and soluble factors can all promote tumor cell persistence and growth.

A number of therapeutic strategies exist to treat patients with melanoma, and specific options are suggested depending on disease state (Table 1.1). If found early, surgical removal of a melanoma can inhibit tumor spread, providing the only “cure”. Beyond surgery, radiation is a common strategy to suppress disease progression. While radiation decreases tumor size, it causes many undesirable side effects in patients and does not necessarily prolong life expectancy [15]. Immunotherapy is a newer strategy that is growing in popularity, with more drugs becoming available in clinical trials. While studies are ongoing, melanomas have been shown to shrink, and a small population of patients have experienced remission; however most tumors eventually become resistant to immunotherapeutics, as occurs with targeted therapy [16–18].

Targeted therapy is standard of care, as selective small molecule inhibitors against BRAF and MEK, which are key players in the MAPK pathway, have prolonged patient lives in late stages. However, tumors can ultimately become resistant to these inhibitors through a variety of mechanisms, which are still under investigation.

For patients with late stage melanoma, chemotherapy remains one option for prolonged survival. Chemotherapy is not the most desirable treatment for patients, since it is extremely taxing, causes a number of horrible side effects, and resistance is still common in late stages [15]. While some labs are already using intravital imaging to interrogate the effects of chemotherapy in vivo, it remains unclear how tumors develop resistance to drug over a long period of time [19]. Therefore, it is critical to identify mechanisms that cause resistance to all types of therapeutics so that we can develop new treatment strategies for patients with metastatic melanoma, especially in later stages. To do this, we must develop animal models of melanoma that are able to fully reproduce the stages of tumor progression and resistance to therapy.

1.5 Modeling melanoma in mice

The characteristics of melanoma development and resistance to therapeutics remain difficult to study, as there currently exist few models of melanoma that properly mimic this process in vivo as it occurs in patients. Current commonly used models of melanoma growth, metastasis, and drug response only touch on some of the true aspects of melanoma progression (Table 1.2). For example, tail vein injection models are still the gold standard in assessing a tumor cell line's metastatic potential. However, this model assesses up to one million tumor cells' ability to colonize in the lungs within a short period of time, and does not properly recapitulate the intricate stages that a single tenacious melanoma cell must accomplish to reach and colonize tissue in a secondary location.

A variety of mouse strains are used in murine tumor models. For most transplant models, where melanoma cells are injected into the animals, immune-compromised mice must be implemented to ensure that the implanted cells are not cleared by the immune system, which

would defeat the purpose of the study. There are four classes of immunodeficient mice that can be used in these studies [20]. “Nude” mice are homozygous for the *Foxn1*^{nu} mutation, which is required for both hair follicle and thymic development. Loss of this gene results in mice that lack T-cells, which are critical players in adaptive immunity. Though not always the most reliable in tumor take rate, nude mice are arguably the most popular of the four classes, as they have an intact innate immune system and are the least expensive. “Scid” mice, homozygous for the *Prkdc*^{scid} mutation, which inhibits rearrangement of T-cell receptor (TCR) and immunoglobulin (Ig) genes, lack both T and B-cells. “*Rag*-deficient” mice are very similar to Scid mice, as they also lack both T and B-cells, however this phenotype is achieved through expression loss of both *Rag1* and *Rag2*. Finally, “higher order, multigenic” mice are generated using the Scid or *Rag*-deficient background, but have additional alleles to inhibit both acquired and innate immune function. These mice lack T and B-cells due to their background, but because of additional mutations, they also lack natural killer (NK) cells and loss of macrophage and dendritic cell function. The more immunocompromised the mouse, generally, the higher likelihood that the tumor implantation will successfully grow in the model, which is especially critical in drug studies trying to assess the likelihood of a patient tumor to respond to a specific therapeutic. However, use of these mice for in vivo tumor studies is problematic, as the complex tumor microenvironment plays a significant role in the overall function and survival of patient tumors. There remains a substantial need for mouse models that properly mimic endogenous tumor formation and drug response in an immune-competent setting to classify and inform therapeutic efficacy.

While there already exist a significant number of mouse models that can recapitulate certain aspects of tumor biology and behavior in vivo, there’s a significant need to improve these models to more precisely mimic clinical settings (Table 1.2). To achieve this, mouse models should provide precise spatiotemporal control of tumor initiation and growth in an endogenous and immune-competent setting, they need to enable long-term longitudinal studies

of drug response, through to the point of tumor resistance and regrowth on drug, and they should be readily coupled with molecular profiling techniques to asses and identify important players in resistance mechanisms for future targeting. Additionally, the ideal model should enable direct visualization of tumor behavior at the single cell level, which will pave the way to identify key patterns of tumor cell behavior over time throughout development and, ultimately, drug response. Given our expertise in and appreciation for imaging, we thought this could be accomplished via coupling an inducible endogenous mouse model of melanoma to intravital imaging. Spoiler alert: we were right.

1.6 Using intravital imaging to study cancer

Quantitative light microscopy has been one of the fastest growing areas of scientific research over the past two decades. With the identification and genetic use of fluorescent reporters and quickly developing technologies in analytical software and imaging modalities, microscopy has arguably become the most illuminating tool in biological investigations [21–23]. The use and visualization of cell culture systems and model organisms have significantly enhanced our understanding of basic biological functions. While cell culture systems provide direct insight into specific roles for a lab's favorite protein (e.g. actin), these studies are performed outside of the cell's natural endogenous environment. As the field grows, it is becoming increasingly imperative to perform imaging experiments in relevant environments, as the micro- and macro-environment outside of the cell plays a significant role in cellular behavior and can influence scientific findings [24].

With this in mind, neurobiology, immunology and cancer biology fields are swiftly moving toward incorporating intravital imaging platforms and techniques [25]. "Intravital microscopy" is the use of microscopy in living organisms, specifically in live mammalian models (e.g. mice, rats). This is particularly important for studies in tumor biology. Although a tumor mass is primarily composed of the cancer cells themselves, there is an extensive and complex stromal microenvironment that plays a critical role in tumor development, persistence, dormancy and

metastasis. Therefore, while significant information can be gleaned from tumor cell studies in vitro, it is also critical to investigate tumor behavior within the endogenous microenvironment.

Multiple microscopy systems can be used for intravital imaging approaches [26]. First, widefield microscopy, though it is relatively inexpensive and enables quick acquisition, is not ideal because it achieves extremely limited depth in a tissue and readily induces photo-bleaching due to off-focus emissions. Secondly, both confocal and spinning disk systems may be implemented, which provide improvements compared to widefield systems as they have increased spatial resolution and reduced photo-bleaching [27]. These systems are commonly used to image cellular behaviors in subdermal organs through surgically implanted glass windows [28]. Thirdly, multiphoton microscopy, though the most expensive option, provides the best imaging modality for thick tissues as it enables resolution of deeper structures compared to confocal, and provides limited off-target photon emissions and limited photo-bleaching [29].

When imaging in vivo, multiple challenges arise. Through solid tissue, photons from both the excitation beam (laser) and the emitted photons from the sample or region of interest are scattered, and the deeper the targeted tissue is, the more challenging it is to excite and detect emitted photons. If the cells, tissue, or structure of interest is more than 50-100μm below the surface, resolution will be lost unless studies are performed via multiphoton imaging, which enables emission and detection of photons with further penetration depth (up to 500μm). Two-photon microscopy, which is what I used for my studies, relies on two photons with wavelengths in the near infrared or infrared (IR) spectrum, which still may have a variable penetration depth depending on the tissue type. Overall, the more heterogeneous a tissue is, the more readily photons will scatter as different tissue components may have different refractive indexes [30]. If imaging is being performed ex vivo, some of this scattering effect can be alleviated through tissue “clearing” mechanisms and protocols [31].

Led by Keefe Chan, a previous postdoctoral fellow in the Bear lab, we established a two-photon imaging system in mice ears [32]. Using our intravital platform, we can stabilize mice underneath the objective on a heating pad for imaging studies lasting less than three hours at a time, using 1-2% isoflurane (reference Figure 2.2). I have incorporated this system in other collaborative studies, two of which were published in 2015 by the DeSimone lab, and two others now in review [33,34].

An additional benefit to two-photon microscopy is that this modality also enables the second harmonic generation [35]. This allows direct visualization of bundled collagens, myosins, myelin, and lipids with no energy absorption. For my studies, tuning the laser to 1050nm enabled simultaneous detection of bundled collagen through the second harmonic along with the fluorescent reporter tdTomato, which marked the endogenous melanoma cells within the ear dermis. Throughout my dissertation, I will address how I used this two-photon intravital imaging system to investigate the roles and interactions between endogenous melanoma cells and bundled collagen within the dermis of the mouse ear throughout tumor development and response to a targeted therapeutic, MEKi.

1.7 Figures

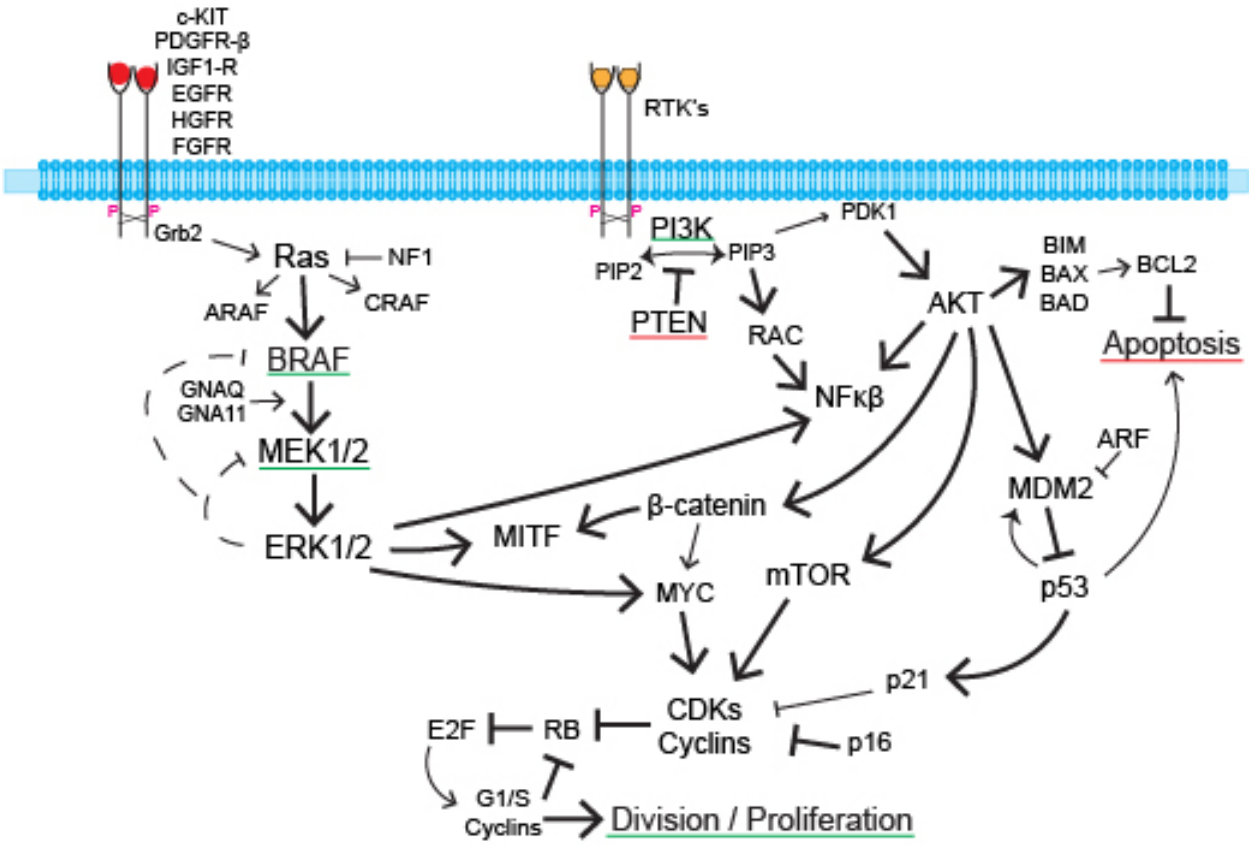

Figure 1.1 Commonly deregulated pathways in melanoma. Activation of receptor tyrosine kinases (RTK's) elicits downstream signaling pathways outlined in this diagram, which play critical roles in cell survival or death. Deregulation of these pathways in melanocytes can induce melanoma development. Items underlined in green suggest proteins or processes that promote melanoma cell growth and survival, while red underlines mark tumor suppressive functions. Underlined items are factors that are highly relevant to my thesis works and are referenced repeatedly throughout this document.

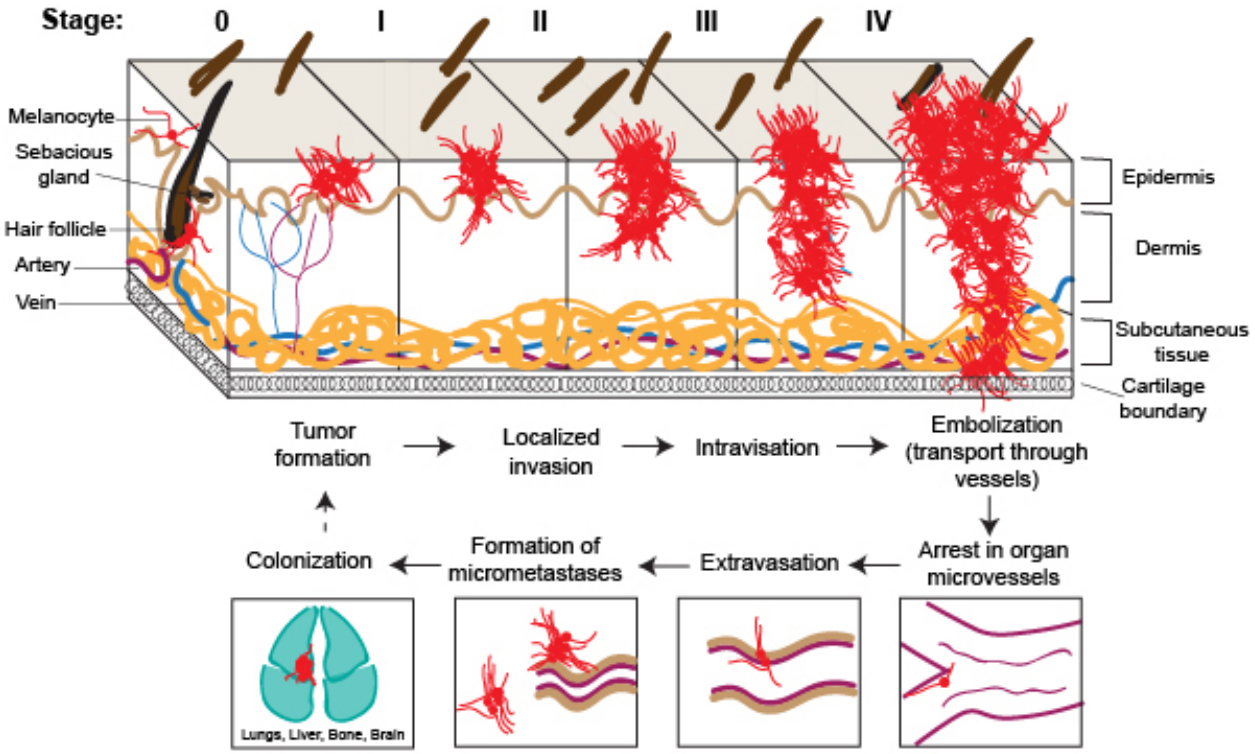

Figure 1.2 Stages of melanoma progression. Graphical representation of melanoma growth within the dermis from a single melanocyte, through to the point of invasion through subcutaneous tissue and the cartilage boundary to undergo hematogenous spread. The different clinical stages of melanoma are represented above each section, “0” representing melanoma in situ, “IV” representing late stage malignancy. The associated steps within the metastatic cascade are also illustrated and outlined.

1.8 Tables

Stage (when?)	Therapy	Details (what?)	Mechanism (how?)	Affected Area (where?)	Side Effects	Prolonged life?
0, I	Surgery	Removal of local tumor & healthy surrounding tissue	1mm tumor: 1cm margin; margin increase with tumor size	local tumor resection	Possible skin graft, scarring	Yes, to normal
	Radiation	External-beam radiation therapy	Use of high-energy X-rays to destroy tumor	local to specific regions	skin irritation, fatigue, lymphedema	Yes
I, II (post-resection)	Adjuvant Radiation	External-beam radiation therapy	Use of high-energy X-rays to destroy tumor	Systemic	skin irritation, fatigue, lymphedema	No
	Adjuvant Immunotherapy	1. Interferon IFNα 2. Ipilumamab (Yervoy)	1. Improve, target, restore immunity 2. Targets CTLA4 enhance T-Cells	Systemic	fatigue, fever, chills vomiting, headache rashes, hair-thinning autoimmunity, rash	Unknown, studies ongoing
unresectable III, IV	Immunotherapy	1. Ipilimumab 2. Nibolumab, Pembrolizumab 3. Interleukin-2	1. see above 2. Inhibit PD-1, activate T-Cells 3. Activate T-Cells	Systemic	1,2. see above 3. low blood pressure fever, chills, capillary leak syndrom	1. Yes, 10-15% 2. tumor shrinks 25-45% cases 3. <10%
	Targeted Therapy	1. BRAF inhibitors a. Dabrafenib b. Vemurafenib 2. MEK inhibitors a. Trametinib 3. Combination a. Dabrafenib/ Trametinib b. Vemurafenib/ Cobimetinib 4. Kit inhibitors: Dasatinib (Sprycel) Imatinib (Gleevec) Nilotinib (Tasigna)	1. Selective small molecule inibitor of BRAF 2. Selective small molecule inhibitor of MEK1/2 3. Selectively inhibits MEK1/2 and BRAF 4. Inhibits KIT gene	Systemic	1. rash, hair thining, dry skin, joint pain, sun sensitivity, fever, nasuea, fatigue, squamous cell carcinoma 2. rash, itching, nail irritation, diarrhea 3. Fever, chills, rash fatigue, vomiting, diarrhea, joint pain, liver problems 4. Studies ongoing	1. Yes, >1year 2. Yes, more than chemo 3. Yes, studies ongoing 4. Studies ongoing
	Intralesional Therapy	1. Talimogene laherparepvec (TVEC)	Engineered herpes virus, infects melanoma & promotes immunity	Local injection	Studies ongoing	Tumor shrinkage, studies ongoing
	Chemotherapy	Dacarbazine, Cisplatin, taxanes, Fotemustine, Lomustine, Vinblastine	Destroy cancer cells via blocking growth & division	Systemic, IV or oral drug	fatigue, infection risk vomiting, hair loss appetite loss, diarrhea, nerve damage	Tumor shrinkage, 12-15% cases, studies ongoing

Table 1.1 Current treatment strategies for patients with melanoma.

Model	Mouse Type?	Can use human cells?	# of Cells?	Spatial & temporal control?	Mimics invasion & metastasis?	Mimics drug response / resistance?	Can couple to intravital imaging?
Xenograft (subcutaneous)	SCID or Nude	Yes	Varies; cells or primary tumors	No; wide variation	No	Yes / No	No
Xenograft (humanized)	NOD/SCID; humanized via bone marrow	Yes	Varies; cells or primary tumors	No; wide variation	No	Yes / No	No
Orthotopic injection (cell suspension)	Nude, or immune-competent	No	~500,000	No	Yes, invasion	Yes / No	Yes
Orthotopic implantation (spheroid)	Nude, or immune-competent	No	3,000 - 7,000	Yes	Yes, *both	Yes / *Likely	Yes
Tail Vein Injection	SCID or Nude	Yes	~1-5 million	No	Yes, intravisation colonization	No / No	No
Spontaneous GEMM	immune-competent	No	Endogenous, varies	No	Yes, distant colonization	Yes / No	No
Inducible GEMM	immune-competent	No	Endogenous, varies	*No	Yes, but 1°'s mistaken for mets	Yes / *No	*No

(*) - Denotes systems we have improved to model the specified variable; studies ongoing or unpublished

Table 1.2 Existing mouse models for melanoma research. List of different types of mouse models that are commonly used to study cancer. Each has deficits in mimicking human disease; highlighting the need for improved models.

CHAPTER 2: BRINGING INTRAVITAL IMAGING TO A GEM MODEL OF MELANOMA ENABLED DIRECT VISUALIZATION OF TUMOR DEVELOPMENT AND IDENTIFICATION OF FACTORS IN EARLY RESISTANCE TO THERAPY

This work is being submitted to the journal *Cancer Research*. Hailey Brighton designed experiments and performed the intravital imaging, histology preparation and imaging, data analysis, and prepared the manuscript. Steve Angus designed and performed the MIB/MS and mRNA-seq experiments, molecular data analysis, western blotting, and helped prepare the manuscript. Kubra Karagoz, Noah Sciaky and Michael L. Gatza performed molecular analysis of mRNAseq data. James Bear guided overall experimental design, data interpretation and helped prepare the manuscript. Tao Bo and Alicia Tagliatela helped with animal experiments. Jose Roques and David Darr helped with animal development and provided Trametinib for our experiments. Norman Sharpless and Gary Johnson were involved in the study design and interpretation of results. James Bear guided experimental design, data interpretation, helped prepare the manuscript, and funded this work.

2.1 Overview

While existing targeted therapies (Trametinib, Dabrafenib, and Vemerafenib) against malignant melanoma have extended patient lifespan overall, melanoma inevitably becomes resistant to drug and disease progresses. This process of drug resistance remains a huge black box in cancer research. For my primary thesis work, I focused on interrogating the effects of Trametinib, a selective small molecule inhibitor of MEK1/2, on endogenous tumor behavior in vivo. To directly visualize melanoma development and drug response at the cell level in situ, we genetically incorporated a tdTomato fluorescent reporter allele into an existing inducible GEM model of BRAFV600E / PTEN-null melanoma. I developed a precise application method of 4-

HT, which enabled spatial and temporal control of melanoma growth in a reproducible fashion, and I performed longitudinal imaging studies of tumors via two-photon intravital microscopy. By treating mice with MEKi over the course of three months, I was able to identify adaptive changes within the spatial relationship between tumor cells and bundled collagen for persistent survival on drug. Furthermore, molecular analysis of tumors at early and late stages on MEKi via mRNA-sequencing and MIB/MS enabled us to identify plastic changes in kinome activity and protein expression during melanoma response to MEKi.

2.2 Introduction

Activating mutations in the MAPK pathway drive malignant transformation in melanoma, with BRAF(V600E) being the most common driver in patient settings [36–38]. Clinical use of selective MEK and BRAF inhibitors have extended life expectancy in patients with malignant BRAF-mutant melanoma and are now the standard of care (Flaherty. *et al.*, 2012; Long *et al.*, 2014; Wellbrock and Arozarena, 2016). However, long-term success of targeted therapy is limited, as tumors ultimately become resistant and disease progresses, even in patients given BRAFi/MEKi combination therapies (Karimkhani, Gonzalez and Dellavalle, 2014; Larkin. *et al.*, 2014; Long *et al.*, 2015). Melanoma can become refractory to therapy via a variety of acquired mechanisms. For one, PI3-K and AKT pathways can increase activity, bypassing the need for MAPK to inform the cell to proliferate [44]. Additionally, enhanced expression of receptor tyrosine kinases, such as c-KIT, FGFR and EGFR may occur, and BRAF variants such as CRAF and ARAF may compensate for loss of BRAF activity [45,46]. However, there still exists a substantial need for relevant preclinical models to analyze therapeutic response *in vivo* in order to make better prognostic predictions and to inform treatment strategies [47].

A complex variety of genomic, epigenetic and extracellular factors all affect how melanoma responds to and resists therapeutic intervention. Evidence of “phenotype switching” at the molecular level has also been identified as a relevant mechanism for how tumors become

resistant to targeted therapy [48–50]. Via this mechanism, tumor cells may adapt a stem-like phenotype, and a "switch" from epithelial to mesenchymal phenotype has been documented in a variety of tumors in response to drug, which is thought to promote malignancy and therapy resistance (Roesch, 2016).

Melanoma cell heterogeneity, which is driven by both switches in molecular expression and changes in the extracellular microenvironment, also influences therapeutic resistance (Straussman *et al.*, 2012; Smith *et al.*, 2014; Roesch, 2015). Exactly how the extracellular matrix (ECM) affects tumor response to drug remains unclear. It is known that collagen in tumors is commonly cross-linked in linear bundles, which can stiffen the microenvironment and elicit downstream signaling events that promote tumorigenesis [54,55]. Improving our understanding of how therapeutics influence the ECM within the tumor microenvironment is critical, as collagen deposition and reorganization may promote melanoma cell invasion, malignancy and resistance through multiple mechanisms [56,57]. Furthermore, intratumoral regions with high stromal cell concentrations have been shown to promote tumor cell persistence against BRAF inhibitor (Hirata *et al.*, 2015). Modeling ECM behavior in tumor development and drug response through proper in vivo strategies can help uncover new therapeutic approaches and targets [59].

To address the challenges of modeling response and resistance to targeted therapies, we have extended an existing *Tyr::CreER; BRAF^{CA};PTEN$^{lox/lox}$* (PBT) GEM model of melanoma by crossing in a lox-stop-lox tdTomato fluorescent reporter allele (tdTomato^{LSL}) [7,60]. The incorporation of this allele enables direct tracking of endogenous melanoma development over time through noninvasive intravital imaging, as well as imaging therapeutic response. With a highly-localized application method of 4-Hydroxy-tamoxifen (4-HT) on the mouse ear, we have achieved precise spatiotemporal control of melanoma initiation. Using this approach, we directly visualized tumor and collagen reorganization throughout development and response to

Trametinib (MEKi), and identified changes in molecular behavior through transcriptome and kinome reprogramming analysis at early and late stages on MEKi.

2.3 Results

A Specific 4-HT-application method enables spatiotemporal control of tumor growth

While inducible Genetically Engineered Murine (GEM) models of cancer have enhanced our understanding of tumor biology and therapeutic response, there exists a significant need to improve these models for translational research [61]. The ability to control endogenous tumor initiation in time and space is a critical experimental variable that needs to be improved to better model melanoma as it occurs in patients. We developed a precise induction method, where 1μL of 20mM 4-Hydroxytamoxifen (4-HT) was applied to the middle of the mouse ear for 8-10 minutes and carefully removed and washed. We chose to induce melanoma on the ear because the skin of the mouse ear contains a population of intrafollicular melanocytes that more closely mirrors human skin, and the ear provides a flat surface for stable intravital imaging. Our imaging strategy incorporated a tdTomato fluorescent reporter allele ($tdTomato^{LSL}$) in the existing tamoxifen-inducible PTEN-null / BRAFV600E (PBT) melanoma GEM model (Fig. 2.1A). This method of 4-HT application yielded reliable local tumor formation on mouse ears in a reproducible fashion, with tumors forming at 100% success rate (Fig. 2.1B, Fig. 2.2F). Additionally, precise spatiotemporal control of melanoma induction in this GEM model extended animal lifespan (normally limited by multiple primary tumors), which enabled long-term longitudinal in vivo studies of melanoma development and, later, drug response.

Visualizing the process of endogenous tumor progression from early stages has been a relative ‘black box’ in the field, as most existing models cannot be used to track tumor cell behavior over time *in situ*. We used two previously described intravital imaging methods to interrogate tdTomato+ PBT melanoma behavior both at the macroscopic (mm) and microscopic (um) scale using a stereomicroscope and a multiphoton microscope, respectively (Fig. 2.2A, B)

[32]. Using anesthetized animals, we positioned them on a heating pad and stabilized the ear with a custom designed ear clamp during imaging. With multiphoton imaging, we were able to quantify the original number of recombined melanocytes post-induction. Less than 2 days after 4-HT treatment, we identified individual recombined endogenous melanocytes within the dermis (Fig. 2.2). At this stage, we counted the tdTomato+ melanoma cells in a 1.2mm^2 region (140cells/mm^2) and approximated the total number of recombined cells that are initially induced by measuring the average area of the 4-HT droplet (2.77mm^2, n = 20) (Fig. 2.2C, D). We determined that less than 400 melanocytes were recombined in this system using an initial 20mM concentration of 4-HT. Additionally, we identified different populations of recombined tdTomato+ cells, including both intra- and inter-follicular melanocytes within the dermis (Fig. 2.2E arrows). Furthermore, breeding out the Pten$^{lox/lox}$ and BRAF^{CA} alleles yielded a control Tyr::CreER; tdTomato^{LSL} mouse line for comparison with nontumorigenic fluorescent melanocytes, which were dendritic and did not proliferate to form melanoma (Fig. 2.4A).

Next, we imaged PBT melanoma progression from early stages serially over time to characterize melanoma development in this model. Tracking tumors each week post-4-HT-application via transmitted light and fluorescence imaging revealed stages of tumor growth that were reproducible from tumor to tumor at different time points (Fig. 1C). At the macroscopic level, melanoma initially spread radially, forming a palpable tumor mass within 6-8 weeks post-application of 4-HT, and we observed relatively homogeneous tdTomato distribution throughout tumor growth (Fig. 1D). Melanoma growth, measured by tumor depth, was exponential, and there was no evidence of tumor development in other regions on the animal, mimicking human disease (Fig. 2.1E, Fig. 2.2G).

Longitudinal intravital imaging reveals distinct phases of melanoma development

Multiphoton imaging provided a platform to simultaneously visualize tdTomato+ melanoma cells and second harmonic generation (SHG), which enabled detection of the

bundled collagen fiber network in the tumor microenvironment (Fig. 2.2E) [62]. Using the SHG as a guide, we visualized the tumor cells throughout the dermis (depth range of 30 μm to ~200 μm), between the epidermis and the cartilage layer in the middle of the mouse ear. In addition, we identified known structures such as hair follicles, which are evident by their circular structure and a center devoid of fluorescence.

By tracking the tdTomato+ melanoma cells in concert with the SHG, we followed melanoma development from early stages with cellular resolution, and we identified distinct phases of growth (Fig. 2.3A, Fig. 2.3B). During the “proliferation phase”, the first few weeks post-4-HT application, we identified clonal populations of melanoma cells arising directly in the dermis. These regions of concentrated tdTomato+ cells expanded over time to become densely packed pre-tumorous lesions. From there, endogenous melanoma spread radially throughout the dermis, during the “pre“ and “early tumor” phases, where the dermis became dense with tdTomato+ melanoma cells. During this phase, SHG signal was significantly reduced, suggesting degradation of bundled collagen and the extracellular matrix. Here, we also clearly identified the tumor boundary in the ear at the cell level (Fig. 2.4C white line). Finally, the “late tumor phase”, 7+ weeks post-4-HT application, corresponded with the vertical growth phase in patient settings, as melanomas rose above the original flat surface of the ear (Fig. 2.1D, Fig. 2.3A). Fluorescence intensity analysis at these different stages of tumor development further recapitulated our ability to model clinical tumor growth, as tdTomato signal increased and the second harmonic signal decreased over time (Fig. 2.3B, C**).**

To compare our ad-hoc intravital staging series to more traditional approaches, we used classic histology techniques to characterize tumor progression in this model via H&E staining. Consistent with our intravital imaging, tissue thickness increased over time, and infiltration of stromal cell populations and increased tumor cell concentrations were evident (Fig. 2.3D). Masson’s Trichrome (MT) staining further demonstrated the degradation of bundled collagen

post-4-HT application, as collagen staining abrogated over time (Fig. 2.3E). Since the tdTomato signal was conserved after tissue processing for histology, we also performed fluorescence microscopy of histological sections to visualize tumor development at different phases (Fig. 2.3F, 2.4D). With this technique, in the "proliferation phase" two-weeks post-4-HT application, we saw a small population of tdTomato+ cells on the dorsal part of the mouse ear where 4-HT was applied. In the early and late tumor phases, however, we identified vertical growth in both ventral and dorsal regions of the ear, and at 8 weeks post-4-HT application, we identified melanoma cell invasion beyond the cartilage layer in the middle of the ear (Fig. 2.4D).

Through defining distinct phases of melanoma development in situ from the initial time point, our system provides a mechanism to visualize tumor cell behavior in a variety of different investigative platforms. We envision that this system can be used to interrogate distinct and relevant hallmarks of early tumor behavior in vivo, such as tumor angiogenesis, tumor-stroma interactions, and invasion prior to vertical growth [63]. However, since our main objective was to create a model of long-term patient response to therapy, we used this system to probe the longitudinal effects of the selective MEK1/2 inhibitor, Trametinib, on melanoma behavior at the cellular and molecular levels.

Melanoma response to MEKi over time is heterogeneous

Since the mechanisms of resistance to BRAF inhibitors in BRAF-mutant melanoma have been thoroughly investigated in other models, we focused on examining endogenous melanoma response to the selective allosteric MEK1/2 inhibitor, Trametinib. To investigate how targeted therapy affects tumor behavior at the macroscopic and cellular levels in this model, we fed MEKi to mice 8-9 weeks post-4-HT application, beginning at the late tumor phase, and serially imaged melanoma response to drug using intravital imaging. MEKi was incorporated into the food (Research Diets) with a daily dose of 0.3 mpk, and food intake was calculated using the Jackson Laboratory's Phenome Database, as in previous studies [64]. Since tumor development

is spatiotemporally controlled in our model, we were able to extend drug treatment and visualize both PBT melanoma response to MEKi and tumor regrowth (after 12 weeks on MEKi), mimicking tumor response to targeted therapy in patient settings.

Without drug treatment, tumors grew exponentially in a spatially defined region with relatively homogenous tdTomato expression throughout continued growth (Fig. 2.5A, C). Tumors responded quickly to MEKi treatment, however, with approximately 30% reduction in tumor size within the first week (Fig. 2.5B, D). Given enough time on therapy, disease progressed and tumors regrew, returning to their original size within 12 weeks. Interestingly, tumor response was heterogeneous even at the macroscopic level, with some regions of persistent tdTomato signal and other regions devoid of fluorescence, some of which were re-populated with tdTomato+ cells at late stages on MEKi (Fig. 2.5B arrows). These results suggest evidence for both intrinsic and acquired functional resistance to MEKi in this model and demonstrate that drug response is heterogeneous.

MEKi induces intratumoral reorganization

We sectioned tumors at early and late stages on MEKi for histology and found changes in tumor cell organization and melanin expression over time, through brightfield and fluorescence imaging (Fig. 2.5E). Before drug treatment, tumor cells aggregated within the dermis but aligned with elongated and spindle-like morphologies closer to the cartilage boundary (Fig. 2.6A, B top panel). Early on MEKi, we identified intratumoral nests within the dermis, where tumor cells organized in a dense circular fashion (Fig. 2.6B middle panel, C). Tumor nests have been described as regions of promoted growth in melanoma, and at this stage on MEKi, they may indicate structures that promote therapeutic resistance [65]. There was also a reduction in tdTomato+ cells near the cartilage layer, and tumor cells distal from the bulk of the tumor mass were more dendritic compared to pre-drug. At the late stage on MEKi during tumor regrowth, tumor nests were less obvious in the dermis, with elongated and aligned

melanoma cells again near the cartilage boundary (Fig. 2.6B third panel). Interestingly, tumor nests were identified in regions of tumor cell invasion through the cartilage boundary at the late stage on MEKi (Fig. 2.6D). Based on fluorescence imaging of histology sections, the density of tdTomato+ melanoma was enhanced in the late MEKi stage compared to pre-treatment, demonstrating that tumor regrowth was largely due to the tumor cells themselves (Fig. 2.5F, Fig. 2.6B).

Tumor cells co-localize with bundled collagen during initial survival on MEKi

The extracellular matrix (ECM) in tumors is highly dynamic, and de-regulation of collagen crosslinking within the ECM has been shown to play a causative role in cancer pathogenesis [19,66]. We used our multiphoton intravital microscopy system to identify critical changes and dependencies between tumor cells and bundled collagen between early and late stages on MEKi. Before therapy, the second harmonic generation signal (SHG) was low, demonstrating a loss or degradation of ECM in PBT tumors 9 weeks post-4-HT. However, MEKi treatment caused morphological changes and reorganization of tumor cells as early as 3 days on drug (Fig. 2.7A). Strikingly, tdTomato strongly co-localized with SHG during this phase, suggesting that the bundled collagen within the dermis of the ear played a role in tumor cell survival on MEKi (Fig. 2.7A, B). After several weeks of continuous treatment, this spatial correlation between tumor cells and bundled collagen structures remained strong (Fig. 2.7A, B). Furthermore, the tdTomato+ melanoma cell density increased over several weeks on MEKi, demonstrating microscopic tumor persistence prior to tumor regrowth.

In the late stage (6-12 weeks on MEKi), (Fig. 2.5D), the correlation between tumor cells and bundled collagen structures diminished as the tumor regrew. At this stage, we observed a loss in spatial correlation and co-localization between tdTomato and SHG signals, and we identified regions of tumor cells independent of collagen and visa-versa (Fig. 2.7A white arrows). Through co-localization analysis between tdTomato and SHG signal, we were able to

measure this loss in tumor cell association with bundled collagen over time on MEKi (Fig. 2.7B). This suggests that over time, as MEKi loses efficacy and melanoma resists therapy, bundled collagen structures become less critical for tumor cell survival, which may be due to a significant change in tumor signaling or phenotype.

Classical immunohistochemistry staining by H&E and Masson's Trichrome (MT), revealed that extracellular matrix (ECM) deposition was greatly enhanced in the late stage compared to early on MEKi (Fig. 2.7C, 4D blue stain). Bundled collagen may play a significant role in tumor cell survival during the beginning of Trametinib therapy. While the ECM changed in character (deposition, location, concentration, distribution, organization), and bundled collagen increased during Trametinib treatment, the dependency on bundled collagen for tumor cell survival at the individual cell level diminished as treatment continued.

Kinome profiling of the Trametinib response reveals potent MEK inhibition and adaptive kinome reprogramming

Since we were able to visualize changes in drug response at the tumor cell level over time by intravital imaging, we sought to complement these insights by interrogating the molecular changes that occur at during Trametinib treatment. To identify reprogramming events in the kinome in parallel with our imaging studies, we harvested Trametinib-treated and control tumors and performed molecular analysis of tumor response (Fig. 2.8). We employed a chemical proteomics approach (multiplexed-inhibitor bead affinity chromatography coupled with mass spectrometry, MIB/MS) to assess the state of the kinome in our model. The adaptive response to targeted kinase inhibitors can lead to dramatic alterations in signaling and ultimately to drug resistance and tumor progression [67–69]. We have previously used MIB/MS to characterize the adaptive response leading to therapeutic resistance to MEK inhibition in triple-negative breast cancer and lapatinib in HER2+ breast cancer [70,71]. The affinity purification involves a mixture of Type I kinase inhibitors to selectively enrich for kinases based on their

activation state, abundance, and affinity for the inhibitors. Untreated tumors and tumors from mice treated for 1 week (early) or 12 weeks (late) on Trametinib were harvested, snap-frozen, and processed for MIB/MS (Fig. 2.9A). As predicted, loss of MEK1/2 MIB binding (as determined by label-free quantification (LFQ) intensity) was dramatic compared to untreated control tumors and persisted throughout the duration of the experiment (Fig. 2.9B). The MIB binding of BRAF and ERK1/2 was also readily observed by LFQ intensity (2.10 4A-C). These observations confirmed that tumors from the Trametinib-treated mice displayed MEK inhibition coincident with the overall tumor depth decrease.

To gain insight into the global kinome response in this model to MEK inhibition, the kinome data was processed with Perseus software and hierarchical clustering of the log2-transformed LFQ intensities was performed (Fig. 2.9C). Notably, the majority of kinases exhibited a comparative loss of binding in response to Trametinib (Fig. 2.9C, inset). Despite the potent inhibition of MEK, a subset of kinases displayed a pattern of increased MIB binding over time (Fig. 2.9C, inset). These kinases included the RTKs c-KIT and Ephrin type-A receptor 1 (EPHA1), the metabolic kinase FN3K, PTK6, the stress-associated kinase CDK5, and B lymphoid kinase (BLK). While a degree of tumor heterogeneity could be observed in the untreated and early time points, the late group appeared more similar in global kinome behavior. This observation was corroborated by principal component analysis of the kinome profile (Fig. 2.10D). To visualize the magnitude and significance of the kinome changes, volcano plots were generated for the Early and Late Trametinib treated tumors relative to the untreated control group (Fig. 2.9D, E). As expected, MEK1 and MEK2 were strongly significant and MIB binding loss was large in magnitude. In contrast, kinases such as c-KIT, FGFR3, and BLK were most dramatically increased in response to Trametinib. These observations were confirmed via WB of tumor lysates (Fig. 2.9F), including loss of phospho-ERK1/2 and a decrease in total PDGFRβ. In addition, tdTomato levels were comparable across all of the tumors (Fig. 2.12E). This is in agreement with the in vivo tumor imaging showing the presence of tdTomato-positive cells at

this time point (Fig. 2.7). These experiments demonstrate the feasibility of chronological kinome evaluation in our melanoma model. Taken together, these data demonstrate the plasticity of the kinome from our melanoma model, even in response to a potent and selective inhibitor. The adaptive kinome response correlated with our intravital imaging observations and provided a deeper level of insight into endogenous melanoma persistence and functional resistance on MEKi.

Transcriptome analysis reveals plasticity and phenotypic alterations in response to MEKi

To assay changes in gene expression throughout MEKi treatment, we utilized sections of snap-frozen tumors harvested at early and late time points on drug for RNAseq analysis, and we compared expression changes with the adaptive kinome response observed by MIB/MS. As shown in Fig. 2.11A, hierarchical clustering of kinome gene expression in response to MEK inhibition revealed substantial and distinct changes at both early and late time points compared to untreated tumors. To identify differentially expressed kinases, we performed DESeq2 comparing the early and late time points to control tumors and visualized the genes in volcano plots [72]. After one week on Trametinib, the expression of numerous kinases was dramatically altered (Fig. 2.11B). Amongst these changes, expression of *Mek1/Map2k1* and *Mek2/Map2k2* was significantly decreased with *Mek1* levels reduced more significantly and to a greater degree. Other kinases with diminished expression included the poorly characterized serine/threonine kinase *Stk32a*, *Cdk18, Akt3, Epha3,* and *Alk*. In contrast, the tumors harvested after one week of treatment displayed increased expression of the fibroblast growth factor receptors *Fgfr2, Fgfr3,* as well as *Rps6ka1 (p90Rsk),* and *Ddr1,* which we have observed in previous in vitro studies.

At the late time point, *Mek1/Map2k1* and *Mek2/Map2k2* were not significantly altered (Fig. 2.11C). In contrast, the expression of kinases such as *Cdk18, Alk, Akt3,* and *Stk32a* was reduced more significantly and to a greater degree over the course of Trametinib treatment. Another kinase with increased gene expression at the late time point included *Ntrk1*,

neurotrophic receptor tyrosine kinase, which is important for neuron development and survival and may play a similar role in melanoma. Additionally, expression of the non-receptor Src-related tyrosine kinase *Srms*, thought to play a role in keratinocyte proliferation, was increased at the late time point (Fig. 2.11). Distinct from the early time point, the expression of lymphocyte kinases *Itk* and *Zap70* was increased with MEK inhibition. Collectively, the kinome expression data suggested that chronic treatment with the MEK inhibitor, Trametinib, did not result in the sustained transcriptional depletion of *Mek1* and *Mek2*. Instead, tumor persistence and regrowth was dependent on unique and diverse set of adaptive kinases in both the early and late time points.

To directly compare the MIB/MS kinome profiles with RNAseq expression data, we plotted the fold-changes observed in kinome by each assay (Fig. 2.11D, E). At both the early and late time points, the inhibition of Mek1 and Mek2 was almost exclusively pharmacological, as determined by loss of MIB binding. However, the loss of *Cdk18, Epha3, Epha7,* and *Stk32a* was also observed at the transcript and signaling level. Additionally, the RTKs *Met* and *Epha1* were found to increase by both RNAseq and MIB binding (Fig. 2.11D, E), but expression of the RTK *Kit* was only significantly increased in the early stage, but displayed sustained MIB binding throughout MEKi treatment. The B lymphocyte kinase, Blk, exhibited increased binding at the late time point but no change in gene expression. Together, the comparison of RNAseq and kinome data are largely in agreement. The notable distinctions, such as Kit and Blk, further substantiate the notion of a phenotypic shift throughout drug response.

As an additional approach to global analysis, we employed pathway analysis of gene expression signatures [73]. Using a panel of previously published gene signatures derived from human transcriptional profiles, pathway signature scores were derived from the mouse tumors using the shared Homologene ID (Fig. 2.11F). Clustering of the pathway signatures readily illuminated five distinct patterns of pathway activity (Fig. 2.11F, Fig. 2.12 5A-D). High pathway signature scores for Cluster 1 (related to mammary stem cells, basal-type breast cancer, and

fibroblasts) were observed in the untreated control tumors but not in MEKi-treated tumors. Thus, the tumors appeared to shift from mesenchymal-like to epithelial-like expression patterns after 1 week of Trametinib treatment. Additionally, signature scores for pathways associated with immune response (e.g. T-cell, B-cell, CD8) increased in response to Trametinib. Indicative of pro-survival signaling, PI3K and AKT pathway scores were also increased over time. Despite some heterogeneity observed in each group, the signature scores for EMT_up and EMT_down were decreased and increased, respectively, over time on MEKi. Thus, the global pathway analysis corroborated the persistent survival of tdTomato-positive tumor cells we observed and provided stronger evidence for a shift to an epithelial state and immune response during treatment.

As the pathway analysis had suggested a transcriptional response to an epithelial phenotype, we explored the relative expression levels of a subset of EMT-associated genes (Fig. 2.11G). Strikingly, genes associated with epithelial phenotype, such as E-Cadherin, were significantly increased in response to MEKi while those associated with mesenchymal phenotype were reduced. Changes in these EMT-associated genes were sustained during MEKi therapy in the early and late treatment groups. Gene list enrichment analysis by Enrichr reinforced this finding, as genes significantly upregulated at early and late time points were most enriched in the “Epithelium” gene set for Mouse Gene Atlas (Fig. 2.12E-H).

Given the dramatic changes in the transcriptome observed in our model in response to MEKi, we surmised that lineage-specific transcription factors might drive the observed phenotypic shift. Therefore, we investigated the mouse transcription factors as a discrete gene subset (Fig. 2.12H, 2.12I). The Sox family of transcription factors are critical players in neural crest development and have been implicated in melanomagenesis [74,75]. In response to MEKi, we observed a significant upregulation of *Sox21* and downregulation of *Sox5* and *Sox10*. Furthermore, two of the most significantly altered transcription factors at both time points were *Zeb1* and *Grhl2* (Grainy-head-like 2). Interestingly, Zeb1 and Grhl2 have been demonstrated to

participate in an intricate reciprocal regulatory feedback loop that governs EMT in breast cancer [76,77]. As validation of the transcriptome analysis, we performed immunoblotting and confirmed that E-cadherin (Cdh1) and pan-Cytokeratin increased in response to MEKi (Fig. 2.11J).

Analysis of the transcriptome revealed that the adaptive kinome reprogramming and collagen reorganization occur in concert to promote persistence of melanoma cells for long-term survival on MEKi. Additionally, while EMT has been characterized as a potential mechanism for resistance to BRAFi, our gene expression analysis suggests the opposite, with increased epithelial signatures in drug treated tumors compared to control. These data represent a comprehensive view of drug response and highlight a potential importance of tumor cell interactions with the extracellular matrix for resistance to targeted therapy.

2.4 Discussion

We developed a highly localized 4-HT application method in an inducible GEM model that achieved reproducible spatiotemporal control of melanoma development on the mouse ear. We reproducibly tracked melanoma development from initial stages through advanced tumorigenesis, and then achieved long-term longitudinal studies of tumor response to therapy which closely mimics clinical response in patient settings (as summarized in Fig. 2.13).

Our intravital imaging approaches allowed us to observe tumorigenesis from the single cell stage in vivo. We identified several reproducible phases of melanoma development in different animals. Early on, we visualized the development of clonal populations of melanoma cells directly in the dermis, which became densely packed pre-tumorous lesions that spread radially throughout the dermis, as it occurs in humans. By 2 months post 4-HT-application, melanoma grew vertically within the dermis to form palpable and spatially defined tumors.

Through long-term longitudinal studies on MEKi in our melanoma model, we discovered that intratumoral reorganization, of both melanoma cells and bundled collagen, played a significant role in tumor cell survival on drug. The SHG signal tightly correlated with tdTomato+

cells at early treatment stages, suggesting a dependency on bundled collagen for tumor cell survival. In the late stage on MEKi, however, this dependency abrogated at the cellular level, as heterogeneous regions of melanoma cells were present independent of collagen (depicted in Fig. 2.13, “Cellular level”). Structural intratumoral differences at different stages on drug, like the presence of tumor nests in regions of invasion across the cartilage boundary at the late stage on MEKi, could support protective mechanisms that enable long-term survival on drug. Additionally, while direct interaction with bundled collagen matrix was reduced in the late stage on MEKi, there is more collagen within tumors at this stage overall, compared to pre-treatment. These results suggest that the stiffening of tumors due to enhanced collagen deposition and tumor cell reorganization over time may be key switch that triggers tumor cell survival and resistance to targeted therapy.

Furthermore, since tumor development in our model is controlled and temporally reproducible, we provide a more in depth and complete view of molecular plasticity on therapy in vivo. Analysis of our MIB/MS data revealed enhanced activity of the collagen binding receptor DDR1 at the early stage on MEKi, further promoting the idea that collagen promotes tumor cell survival against therapy. Although phenotype switching via “EMT” has previously been described as a means to promote drug resistance, we find evidence of a “MET” progression appears to enhance initial survival of melanoma cells against therapy. Comparing mRNA-seq and MIB/MS data of melanoma tumors in late versus early stages on drug, we have identified c-Kit, EPHA1, CDK5, BLK, PTK6, and FGFR3, as potential drivers of functional resistance to MEKi in this model.

By using a combination of novel approaches in our model system, we set the stage for new discoveries and understanding about tumor biology and therapeutic response. Coupling our imaging studies with transcriptome and kinome reprogramming analysis enables direct interrogation of tumor plasticity *in vivo* during drug response and the identification of properties

and potential therapeutic targets that promote resistance. Using these novel approaches, we have developed a model that enables direct observation of endogenous tumor development, tumor heterogeneity, and plastic response to targeted therapy at the endogenous cell level *in situ*. These methods will advance our basic understanding of the cellular processes involved in disease progression, increase the utility of existing and future GEM models, and aid in the testing of new therapeutics for malignant melanoma.

2.5 Materials and methods

Local 4-HT Application Method

To achieve spatially controlled melanocyte recombination by local topical application, we applied 1µl of a 20mM concentration of 4-HT solution in DMSO, 100% Ethanol and Orange-6 dye (the active ingredient in Henna skin tattoo dye to allow precise visualization of the region exposed to 4-HT in which CreER is activated), to the middle of the ear while the mouse was anesthetized. After 8-10 minutes, the area was vigorously washed with 70% EtOH to prevent transfer of tamoxifen to other areas and to ensure a single, controlled primary lesion (Fig. 2.1B). Using this method, we consistently induced local melanoma growth exclusively in the applied region in a reproducible fashion.

Intravital Two-photon Microscopy

Tumor-bearing animals with tumors between 10-30mm^3 were imaged as previously described [32]. Animals were anesthetized with 1-2% isoflurane on a heating pad equipped with temperature feedback, and tumors were imaged before and during the course of drug treatment studies. All imaging was performed at 1050 nm with an Olympus FV1000MPE mounted on an upright BX-61WI microscope, using a 25x, 1.05 N.A. (2 mm W.D.) water immersion objective with optical imaging gel with the same refractive index as water to capture images. A custom aluminum ear clamp, with 1) a bottom platform on which the ear rests and 2) an upper piece equipped with a pair of thumbscrews to secure the ear underneath a coverslip, facilitated

transfer of heat to the ear from an underlying heating plate/pad during imaging. Laser power (4%), software, and microscope settings (RXD2 and RXD4 channel PMT voltages at 850 and 500, respectively) were consistent for all acquired images. The IR laser unit (MaiTai DeepSee, Sptectra-Physics) is tunable from 690–1300 nm with a pulse width < 100 fs. Two channel non-descan detectors were used for image collection, and data was gathered with the Olympus Fluoview software.

Macroscopic Imaging of tdTomato positive tumors

Macroscopic imaging was performed on an Olympus MVX10 stereoscope system, and images were collected using Metamorph software and a color camera at 0.8X or 1X magnification. Fluorescent images were acquired using a mercury lamp and filter wheel for red fluorescence. Mice were anesthetized with 1-2% isoflurane and placed on a heating pad during imaging. Ears were flattened and stabilized to 5mL tubes with double sided tape to enable full macroscopic view of each tumor.

Histology of tumor progression and tumor response to Trametinib

Ears and lymph nodes were excised and fixed in 4% PFA at 4C for 24 hours. Tissues were then cryoprotected with fresh 30% sucrose at 4C for 24 hours. Ears and lymph nodes were then frozen in VWR Clear Frozen Section Compound (VWR 95057) using an ethanol / dry ice bath and were stored at -80C before sectioning. Sectioning and H&E staining were performed by the Cell Biology & Physiology Histology Core at UNC Chapel Hill.

Drug treatments and further mouse protocols

0.3mpk Trametinib (GSK212) conjugated in chow was fed to mice, which were harvested at 1, and 12 weeks on drug treatment. Tumor measurements were performed with a digital caliper every week during the course of each experiment, and measurements for length, width, and height were recorded (in mm). Tumor size was indicated by tumor depth. Mice were carefully monitored in accordance with our protocol.

Fluorescence Intensity Analysis

Maximum intensity projections were made from z-stacks with 4μm intervals, taken with FV1000MPE two-photon, (roughly 20-40 slices per image, depending on tumor depth). Average intensity was measured using Metamorph software analysis, and the intensity for each image was normalized by subtracting the value for background average fluorescence. Measurements were averaged for each time point, post-4-OHT application, plotted in Excel, and graphed in Prism. Each image was acquired with 4% laser power to maintain consistency.

Multiplexed inhibitor bead (MIB) chromatography and mass spectrometry (MS)

Snap-frozen tumors were crushed by mortar and pestle in ice-cold MIB lysis buffer (50mM HEPES, 150mM NaCl, 0.5% Triton X-100, 1mM EDTA, 1mM EGTA, pH 7.5) supplemented with complete protease inhibitor cocktail (Roche) and 1% phosphatase inhibitor cocktails 2 and 3 (Sigma). Extracts were sonicated 3 x 10s, clarified by centrifugation, and syringe-filtered (0.22um) prior to Bradford assay quantitation of concentration. Equal amounts of total protein (0.3mg) were gravity-flowed over multiplexed inhibitor bead (MIB) columns in high salt MIB lysis (1M NaCl). The MIB columns consisted of 175ul mixture of six Type I kinase inhibitors (CTx-0294885, VI-16832, PP58, Purvalanol B, UNC-21474, and UNC-8088A) custom-synthesized with hydrocarbon linkers and covalently linked to ECH-Sepharose beads as previously described [71]. Columns were washed with 5mL of high salt (1M NaCl), 5mL of low salt (150mM NaCl) MIB lysis buffer, and 0.5mL low-salt lysis buffer with 0.1%SDS. Bound protein was eluted twice with 0.5% SDS, 1% beta-mercaptoethanol, 100mM Tris-HCl, pH6.8 for 15 min at 100C. Eluate was treated with DTT (5mM) for 25 min at 60C and 20mM iodoacetamide for 30 min in the dark. Following spin concentration using Amicon Ultra-4 (10k cut-off) to ~100 uL, samples were precipitated by methanol/chloroform, dried in a speed-vac and resuspended in 50mM HEPES (pH8.0). Tryptic digests were performed overnight at 37C, extracted four times with 1mL ethyl acetate to remove detergent, dried in a speed-vac, and peptides further cleaned using C-18 spin columns according to manufacturer's protocol (Pierce).

RNA isolation, RNA-seq library preparation, RNA-seq and analysis

A center section of each snap-frozen tumor was excised with a clean razor blade and RNA isolated using the RNeasy Plus Mini Kit (Qiagen) according to manufacturer's protocol with the optional DNase I treatment (Qiagen) for 15min. 400ng total RNA was used as input for RNA-seq library construction with a Kapa Stranded mRNA kit according to the manufacturer's protocol. TruSeq adapter sequences were used for indexing. Library amplification was as described with 12 PCR cycles. Equimolar amounts of each library were run as a 12-plex on a NextSeq 500—75 cycle, high output V2 kit. Expected read counts for genes were used as input for DESeq2 to identify differentially expressed genes [72]. Differentially expressed gene sets (padj<0.1) were used as input for Enrichr [78] to identify pathway enrichments. Heat maps of log2 transformed RSEM normalized expression values were generated using GENE-E software (Broad Institute). Normalized RSEM mouse gene values were converted to unique human gene IDs by shared homologene ID.

Western Blotting

Snap-frozen tumors were extracted in MIB lysis buffer (150mM NaCl) as above and filtered lysates were boiled in 1X SDS sample buffer for 10min at 100C. Equal amounts of lysate were separated by SDS-PAGE, transferred to nitrocellulose membrane, blocked with 5% milk in TBS, and subjected to immunoblotting with the following primary antibodies: phospho-ERK1/2 (218/222), MEK1/2, phospho-MEK1/2, LCK, from Cell Signaling; ERK2 from Santa Cruz; RFP (to detect tdTomato) from. Secondary antibodies used were goat anti-Rabbit-HRP or goat anti-mouse-HRP from Pierce. SuperSignal West Pico Chemiluminescent Substrate (Thermo Scientific) was used and images were collected on a Biorad ChemiDoc.

Liquid Chromatography, Mass Spectrometry and Analysis

Peptides were resuspended in 2% ACN and 0.1% formic acid. 40% of the final peptide suspension was injected onto a Thermo Easy-Spray 75µm x 25cm C-18 column and separated on a 180min gradient (5-40% ACN) using an Easy nLC-1000. The Thermo Q Exactive mass

spectrometry ESI parameters were as follows: 3e6 AGC MS1, 80ms MS1 max inject time, 1e5 AGC MS2, 100ms MS2 max inject time, 20 loop count, 1.8 m/z isolation window, 45s dynamic exclusion. Raw files were processed for label-free quantification by MaxQuant LFQ using the Uniprot/Swiss-Prot mouse database. Normalized LFQ intensities were plotted using GraphPad Prism or imported into Perseus software.

2.7 Figures

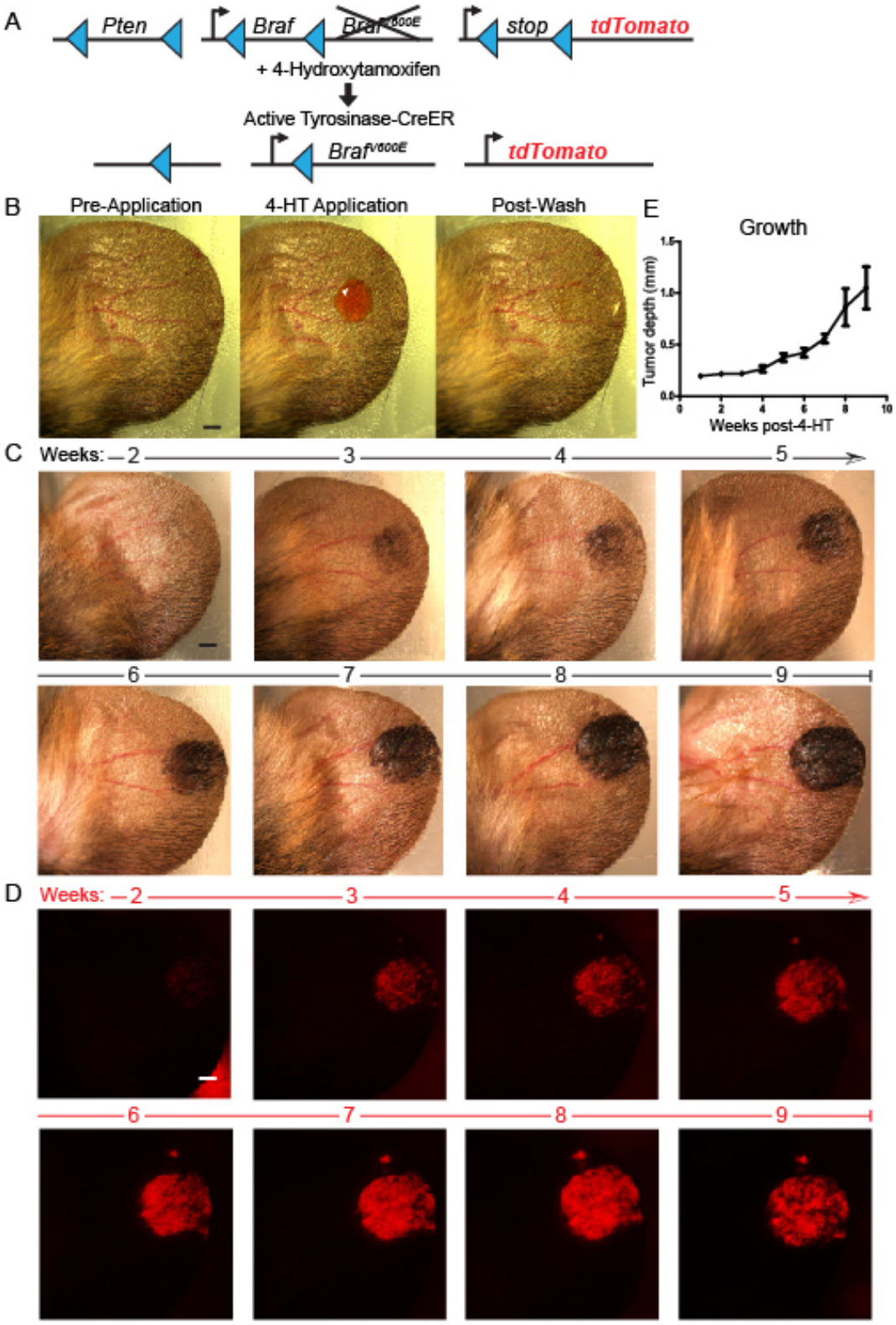
A
Pten
Braf
Braf V600E
stop
tdTomato
+ 4-Hydroxytamoxifen
Active Tyrosinase-CreER
Braf V600E
tdTomato
B
Pre-Application
4-HT Application
Post-Wash
E
Growth
Tumor depth (mm)
Weeks post-4-HT
C
Weeks: 2 3 4 5
6 7 8 9
D
Weeks: 2 3 4 5
6 7 8 9

Figure 2.1. Genetic incorporation of tdTomato enables visualization of melanoma initiation and growth with specific 4-HT application method. A) Diagram of PBT (*Tyr::CreER;BRAF^{CA};PTEN$^{lox/lox}$;tdTomato^{LSL}*) melanoma GEM model pre- and post- CreER-induced recombination. B) Macroscopic images pre-, during, and post- 4-HT application on a single mouse ear. Olympus MVX10. Bar = 500μm. C) Macroscopic images with transmitted light and D) tdTomato fluorescence of tumor growth longitudinally over time on a single mouse ear, 2-9 weeks post-4-HT application. E) Tumor growth, measured by tumor depth, over time. N≥12. Error bars = 95% CI's.

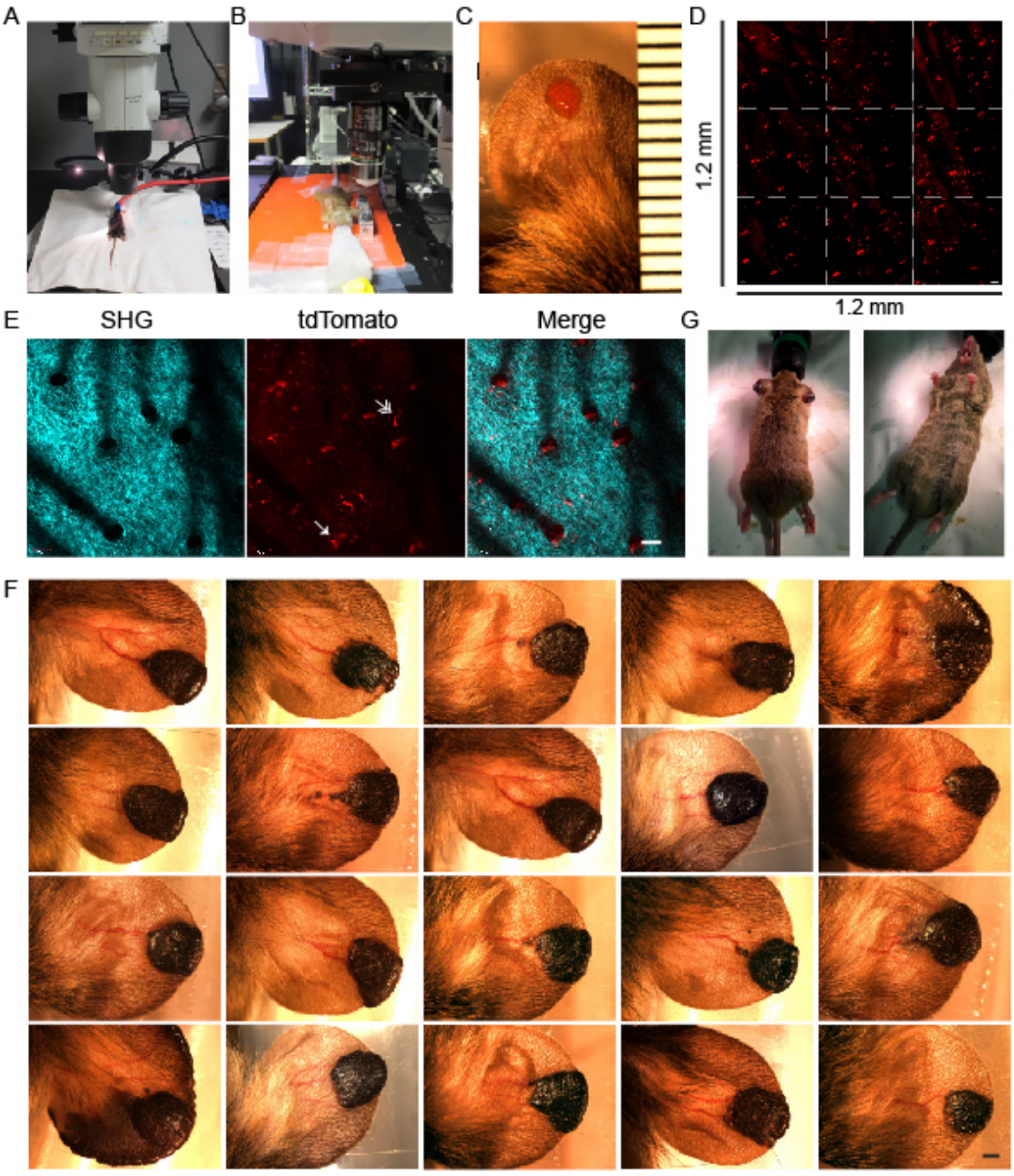

Figure 2.2. Achievement of reproducible spatial and temporal control of melanoma growth with <400 initiating cells. A) Intravital imaging set-up with Olympus MVX10 and B) Olympus FV1000MPE multiphoton. iPhone6 camera. C) 1μl 4-HT droplet, approximately 2.7mm^2. D) 9 max. intensity projections acquired within one 1.2mm^2 region of the mouse ear. E) SHG, tdTomato, and Merge max. intensity projections of the dermis 40hours post-4-HT. Arrows

mark single melanocytes. Olympus FV1000MPE; 1050nm; 4% laser power. Bar = 50μm. F) Panel of macroscopic images with transmitted light of 20 different tumors, all 9 weeks post-4-HT. Bar = 500μm. G) Whole animal, 16weeks post-4HT. Tumors only present on ears.

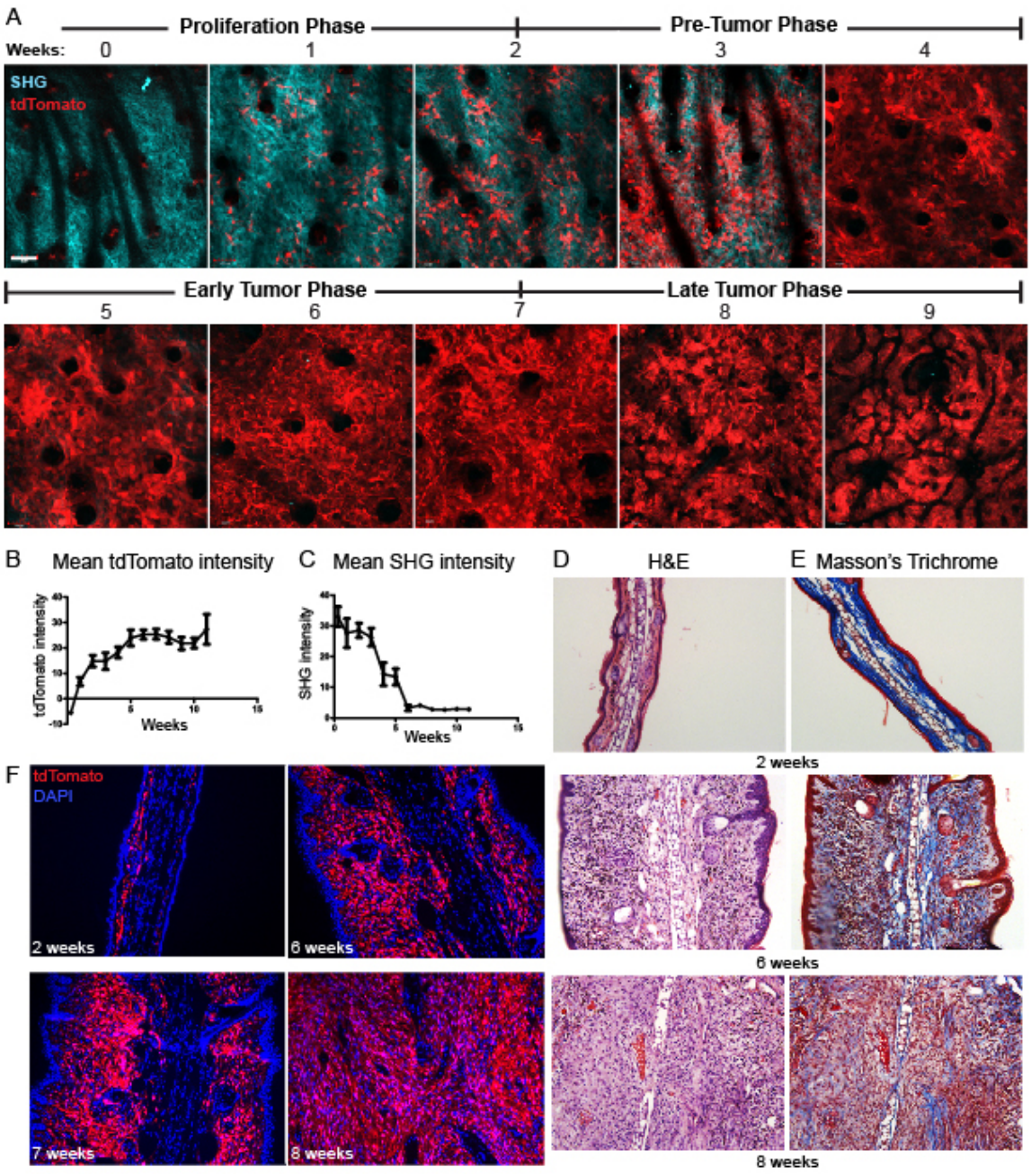

Figure 2.3. Visualizing melanoma development over time with cellular resolution. A) Intravital multiphoton images of tdTomato+ PBT melanoma development in the mouse ear over time; 0-9 weeks post-application of 20mM 4-HT. Second Harmonic Generation (SHG) reveals bundled collagen within the dermis of the ear. Images show merged SHG and tdTomato channels. FV1000MPE; 1050nm; 4% laser power. B) Normalized average intensity of tdTomato signal and C) SHG signal during tumor growth over time. N≥12. D) H&E staining and E)

Masson's Trichrome staining of mouse ears 2, 6, and 8 weeks post-4-HT application. Olympus BX51; 10X Objective; Brightfield. F) Histology of tdTomato+ tumor growth at 2, 6, 7, and 8 weeks post-application of 20mM 4-HT. Images display merged DAPI and tdTomato channels. Olympus BX51; 20X Objective.

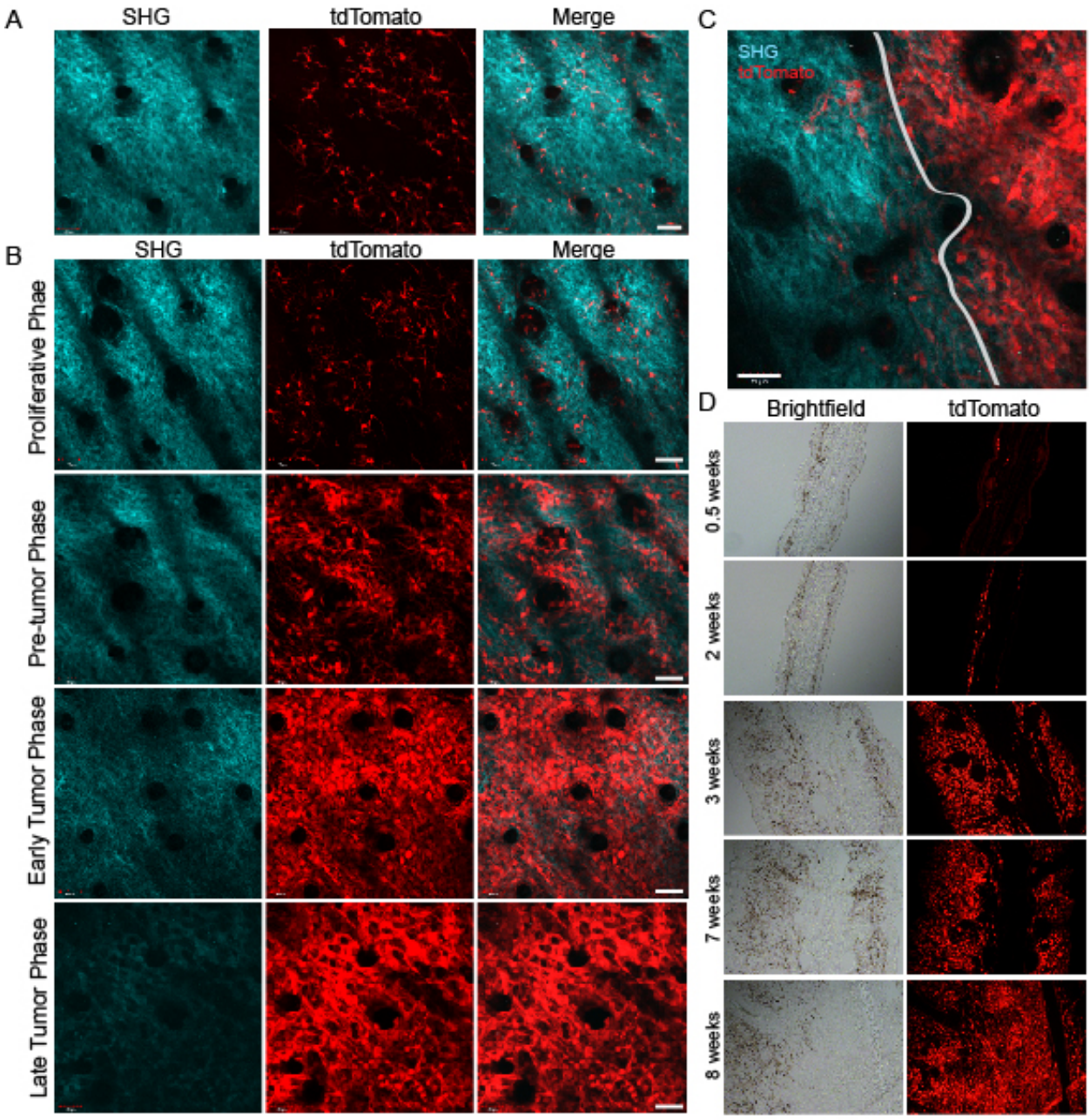

Figure 2.4. BRAF^{V600E} and PTEN-loss are required for tumor growth, which is temporally controlled and reproducible at the cell level. A) Intravital two-photon images of *Tyr::Cre; tdTomato^{LSL}* mouse ear, 2 weeks post-application of 20mM 4-HT. SHG and tdTomato acquired at 1050nm. Maximum intensity projections; FV1000MPE; 25X; 4% power. Scale bar = 50μm. B) Two-photon max intensity projections of PBT tumor development over time at 1, 3, 5, 7 and 9 weeks post-application of 20mM 4-HT. Bar = 50μm. C) Merge of SHG and tdTomato at tumor

boundary in mouse ear, 4 weeks post-4-HT application. FV1000MPE; 1050nm; 25X; 4% power. Bar = 50μm. D) Histology of PBT mouse ears 4 days and 2, 6, 7, and 8 weeks post-application of 20mM 4-OHT. Brightfield and tdTomato fluorescence acquired with Olympus BX51; 20X.

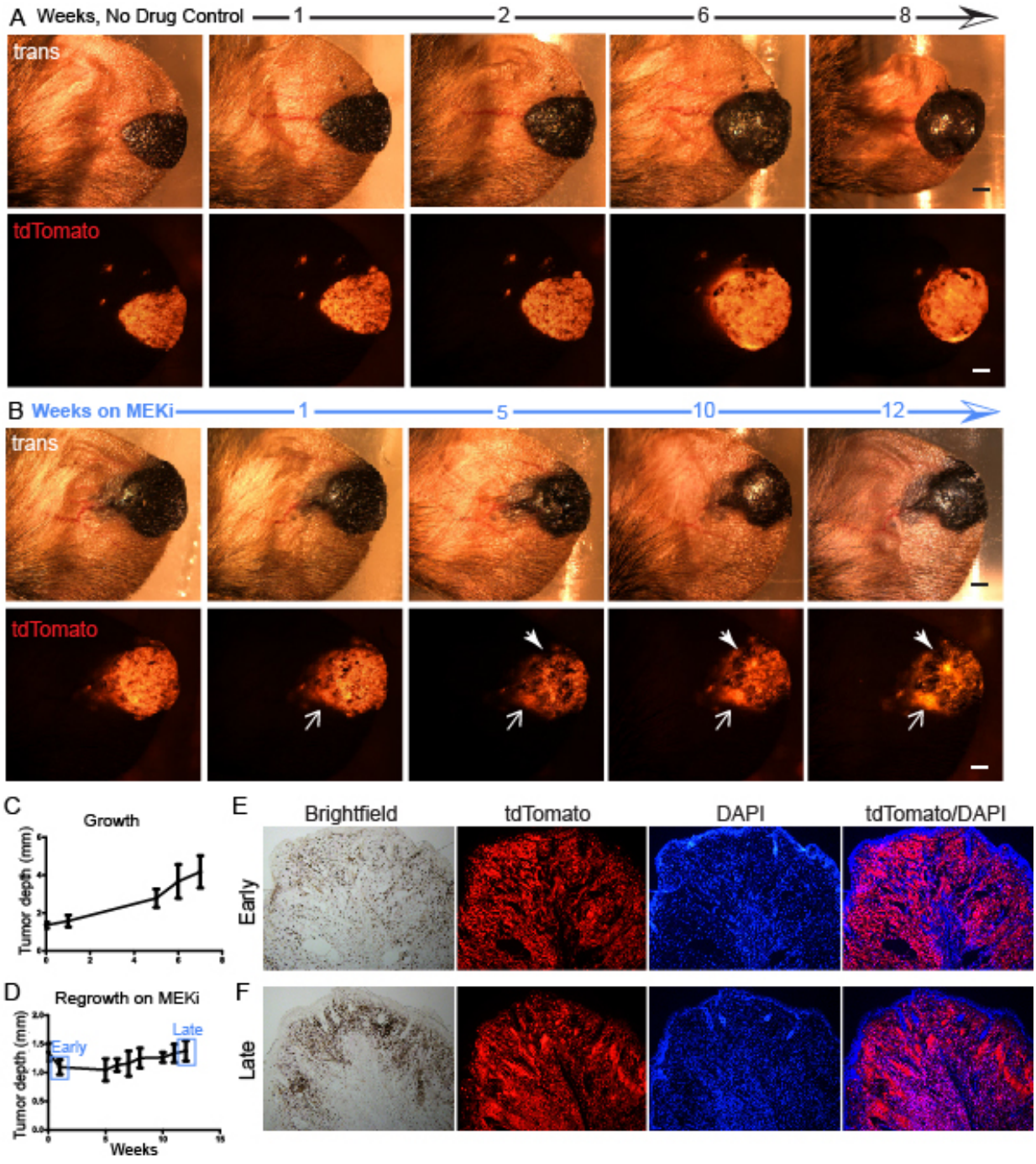

Figure 2.5. Heterogeneous response to MEKi over time. A) Macroscopic images of a PBT tumor without drug treatment 8, 9, 10, 14, and 16 weeks post-application of 20mM 4-HT and B) Macroscopic images of a PBT tumor over time pre- and 1, 5, 10 and 12 weeks on Trametinib therapy. C) Graphical representation of PBT tumor thickness / growth over time without MEKi Trametinib treatment and D) over time on MEKi therapy. N= N≥4. Error bars = 95% CI. E)

Histology of tdTomato+ PBT tumor response to Trametinib at 1 week (early) and 7 weeks (late) on drug. Brightfield, DAPI, and tdTomato fluorescence acquired with Olympus BX51; 10X.

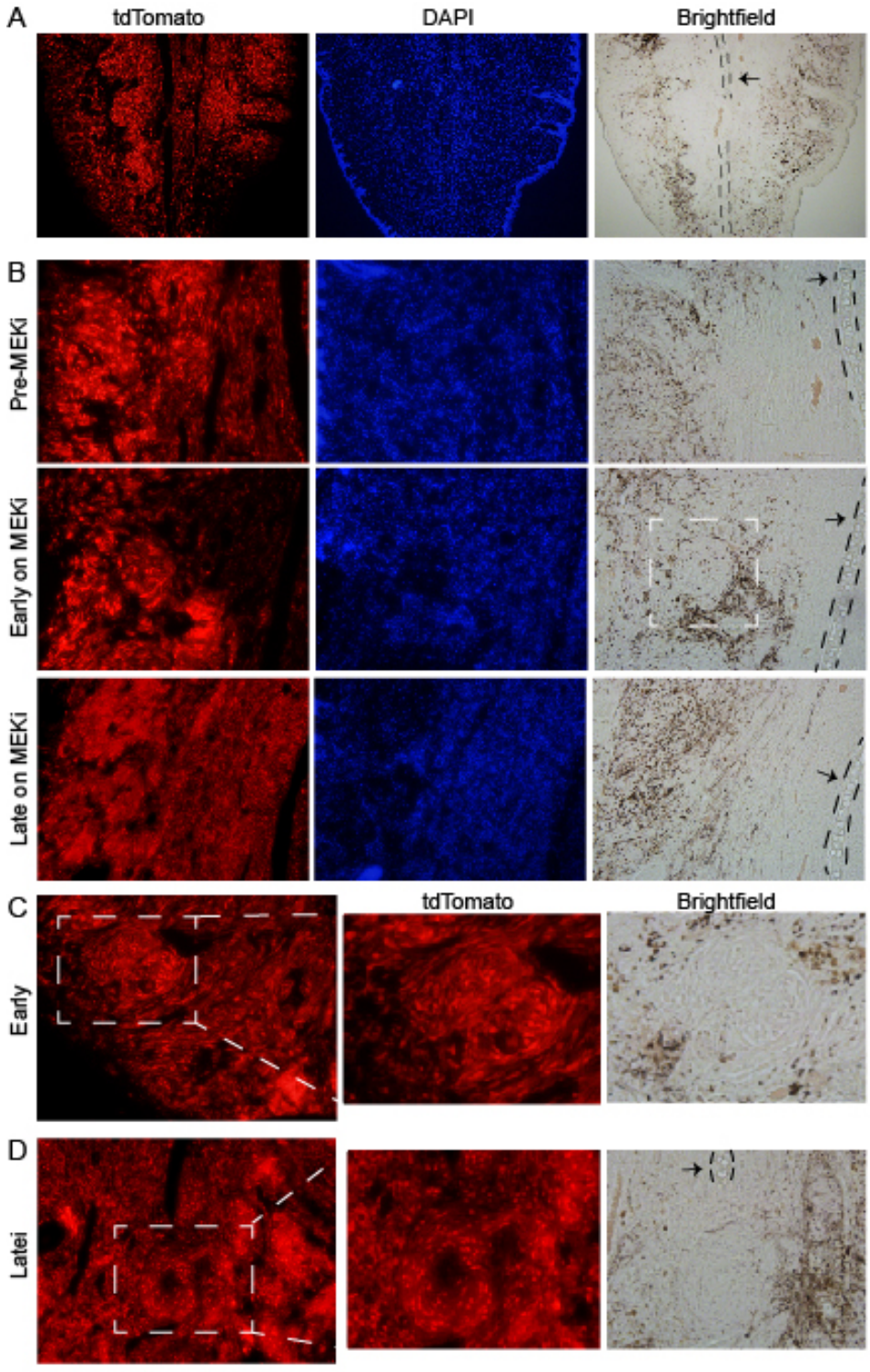

Figure 2.6. Amelanotic intratumoral nests are evident in persistent melanoma cell populations on MEKi. A) End-on view of melanoma ear tumor 8 weeks post-4-HT application

with tdTomato, DAPI, and bright field. 7µm thick section. Olympus BX51, 10X objective. B) tdTomato, DAPI, and bright field images of tumors pre-, 1 week, and 7 weeks on MEKi therapy. Olympus BX51; 20X. C) 20X and zoom of tumor section 1 week on MEKi and D) 7 weeks on MEKi.

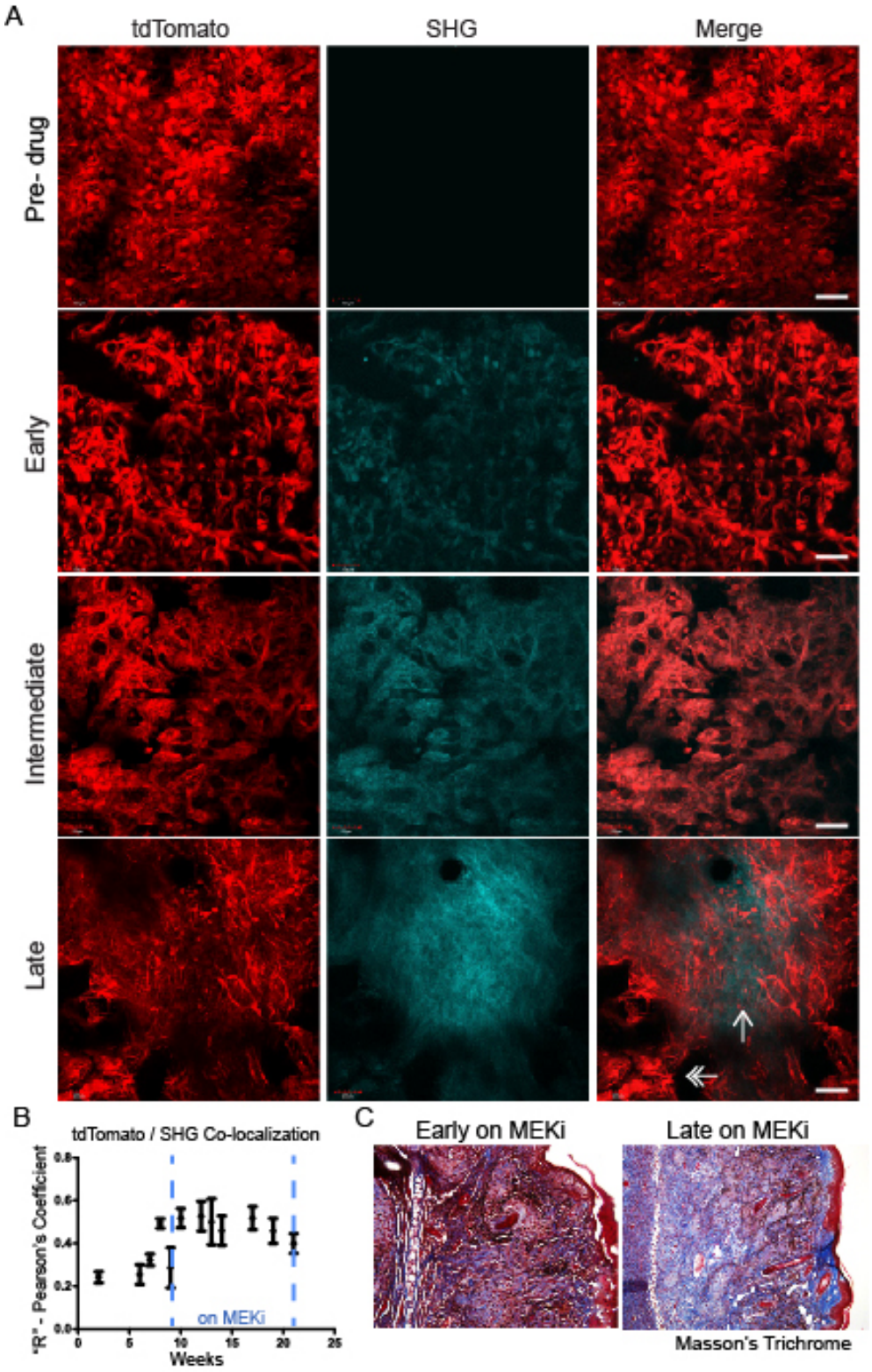

Figure 2.7. Intravital imaging reveals a relationship between bundled collagen and tumor cells for survival on MEKi. A) Intravital multiphoton imaging of tdTomato+ PBT melanoma

response to MEKi pre- treatment and at early (3 days), intermediate (3.5 weeks), and late (9 weeks) stages on drug. Maximum intensity projections; FV1000MPE; 25X; 1050nm; 4% power. Scale bar = 50μm. B) Average Pearson's correlation coefficients for SHG and tdTomato signals over time on MEKi treatment. N≥9. Error bars = 95% CI. C) Masson's Trichrome (MT) staining of histological slices of PBT melanoma at early and late time points (1 and 7 weeks) on MEKi. Blue signal represents intratumoral ECM and bundled collagen.

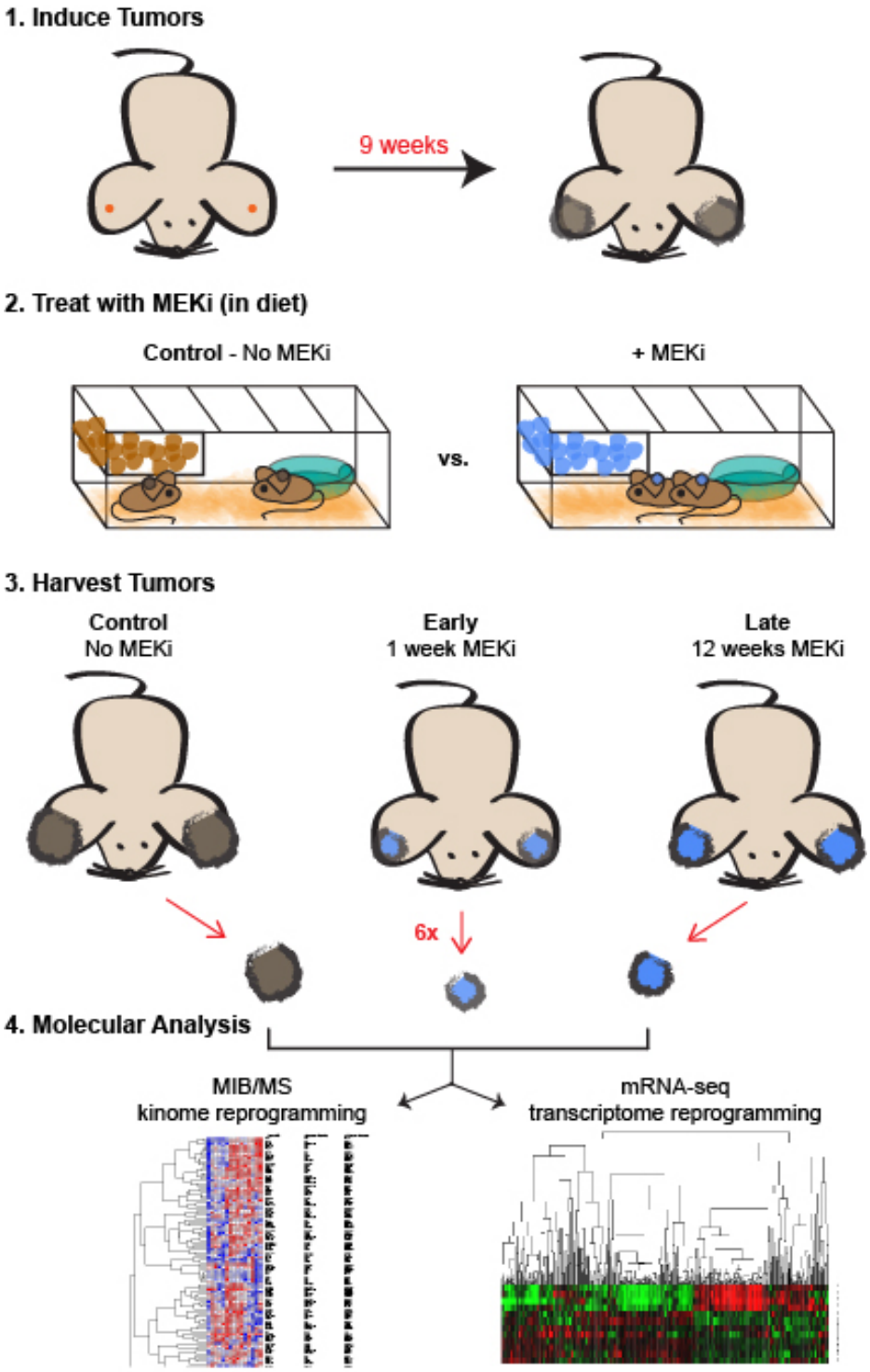

Figure 2.8. MEKi Experiment Overview. Graphical representation of the experimental design for longitudinal treatment and molecular analysis of melanoma response at early and late stages on continued treatment with MEKi (0.3mpk), compared to no drug control. Orange dots in (1)

represent 4-HT application, circular shapes represent no drug control (gray) and MEKi treated (blue) tumors. 6 tumors for each condition (no drug control, early, and late on MEKi) were harvested for molecular profiling. MIB/MS and mRNA-seq images are representative of results from this experiment but are not the actual data.

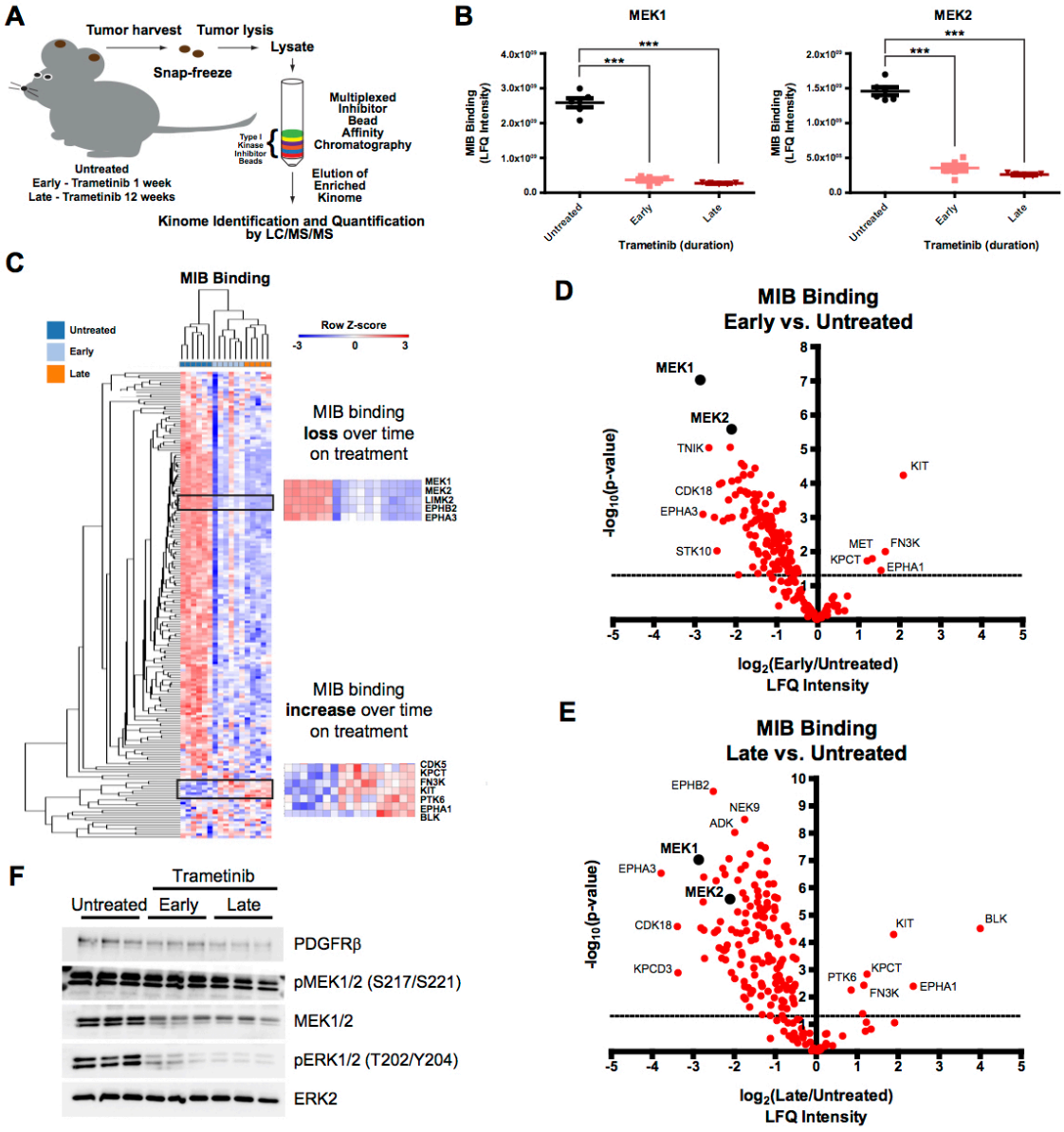

Figure 2.9. Adaptive kinome response to chronic and potent MEK inhibition. (A) Schematic representation of experimental MIB/MS workflow. (B) MIB binding (LFQ intensities) for MEK1 and MEK2 from untreated, early, and late tumors. ***, p<0.001. (C) Hierarchical clustering displayed as a heat map of mean-centered, log_2-transformed LFQ intensities (MIB Binding) form untreated, early, and late tumors as in (A). Select panels are indicated and labeled with kinases by row. (D) Volcano plot showing log2 fold-change MIB binding (LFQ intensity) for early versus untreated tumors plotted against the –log10 p-value (FDR=0.05).

Dotted line, p=0.05. (E) Volcano plot showing log2 fold-change MIB binding (LFQ intensity) for late versus untreated tumors plotted against the –log10 p-value (FDR=0.05). Dotted line, p=0.05. (F) Western blots for untreated, early, and late tumors as in (A). ERK2 was used as a loading control.

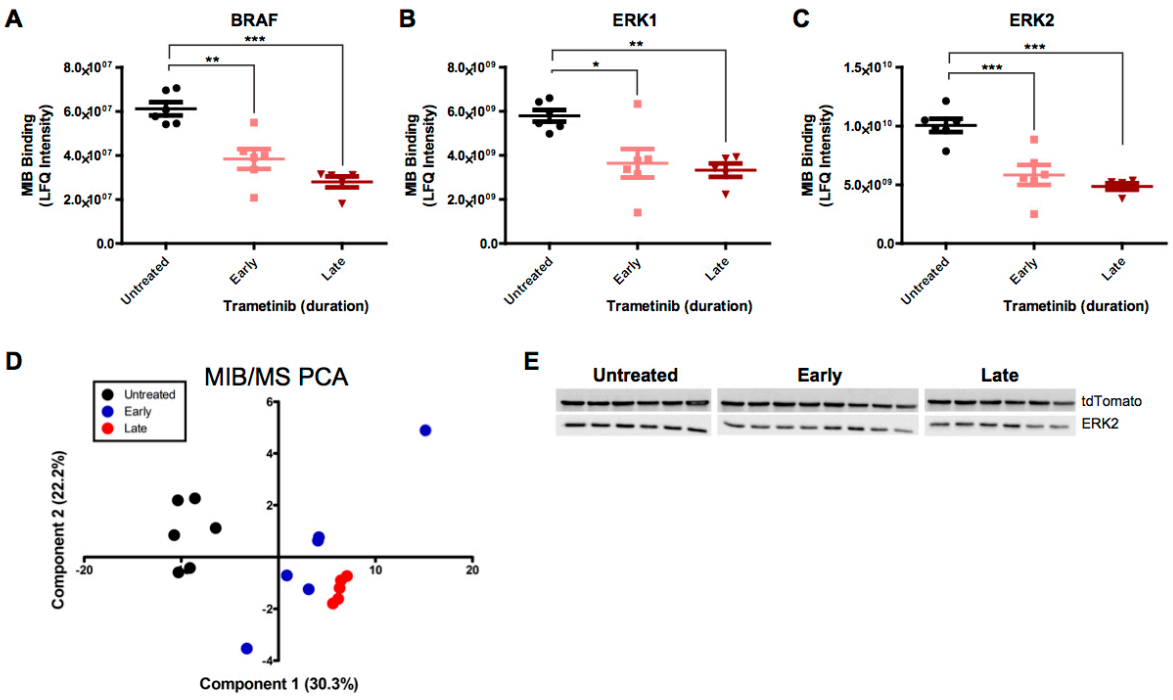

Figure 2.10. MEKi inhibits MAPK pathway throughout drug treatment. (A, B, and C) MIB binding (LFQ intensities) for (A) BRAF, (B) ERK1 and (C) ERK2 from untreated, early, and late tumors described in Fig. 5A. ***, p<0.001 (D) Principal component analysis of $\log_2$ (LFQ intensity) for kinases identified by MIB/MS in untreated and early and late Trametinib-treated tumors. (E) Immunoblotting to detect tdTomato expression from tumor lysates from untreated, early, and late tumors. ERK2 was used as a loading control.

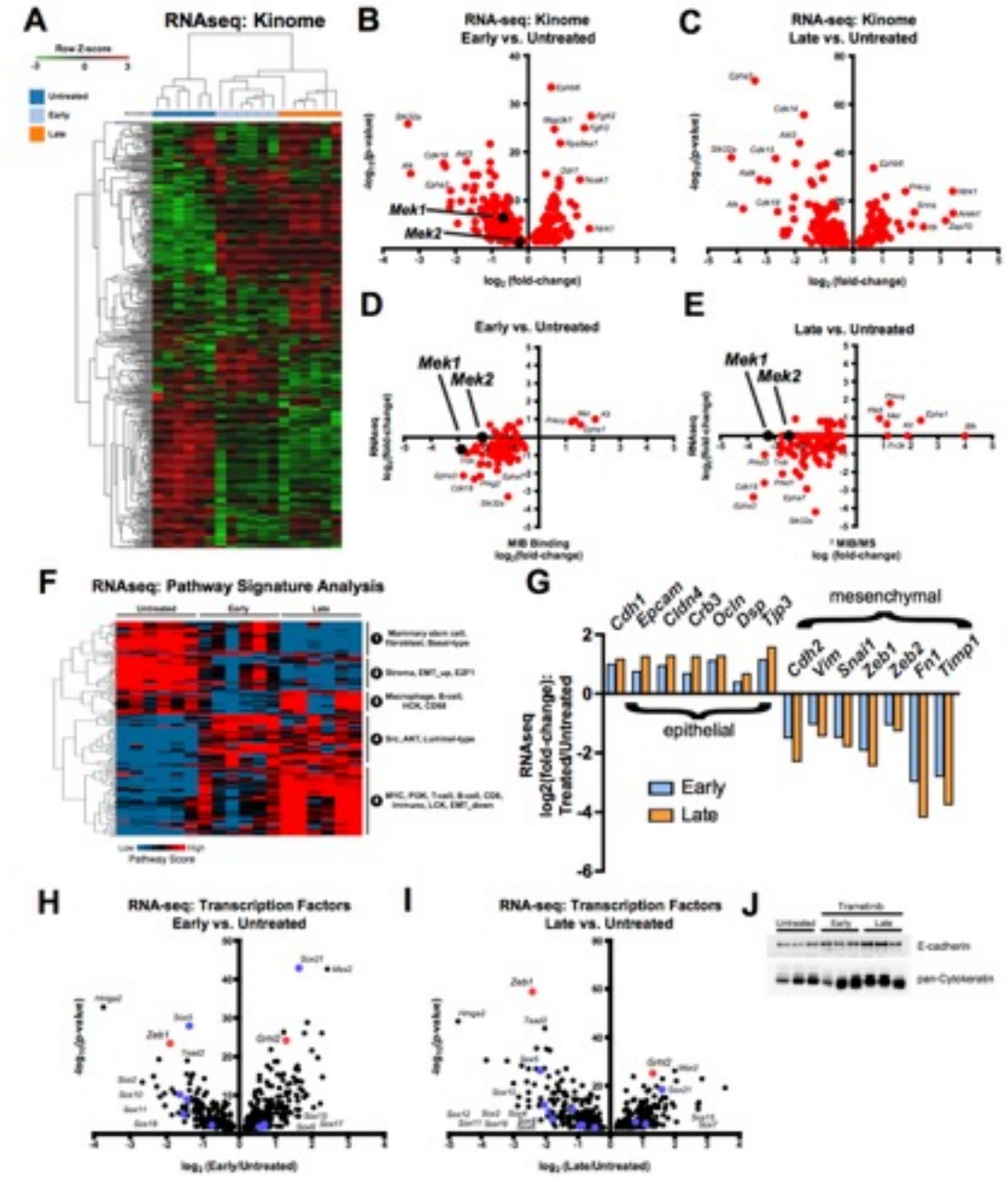

Figure 2.11. Transcriptome profiling reveals dramatic phenotypic shift in response to Trametinib. (A) RNAseq analysis of untreated, early, and late tumors as log2-transformed RSEM normalized gene counts. Hierarchical clustering displayed as a heat map of the mean-centered mouse kinase genes. (B) Volcano plot showing log2 fold-change (RNAseq) for early versus untreated tumors plotted against the –log10 p-value (FDR=0.05) as determined by

DESeq2. Dotted line, p=0.05. (C) Volcano plot showing log2 fold-change (RNAseq) for late versus untreated tumors plotted against the –log10 p-value (FDR=0.05) as determined by DESeq2. Dotted line, p=0.05. (D) Log2 LFQ intensities (MIB binding) and Log2 RNAseq expression changes (early versus untreated) are plotted for kinases quantified by MIB/MS. (E) Log2 LFQ intensities (MIB binding) and Log2 RNAseq expression changes (Late versus Untreated) are plotted for kinases quantified by MIB/MS. (F) RNAseq data from untreated, early, and late tumors were used for Pathway Signature analysis and clustered. Representative signatures from each cluster are indicated at right. (G) Log2 fold change as determined by DESeq2 for select genes involved in EMT. (H) Volcano plot as in (B) for transcription factor genes. (I) Volcano plot as in (C) for transcription factor genes. (J) Western blots for indicated proteins from untreated, early, and late tumors.

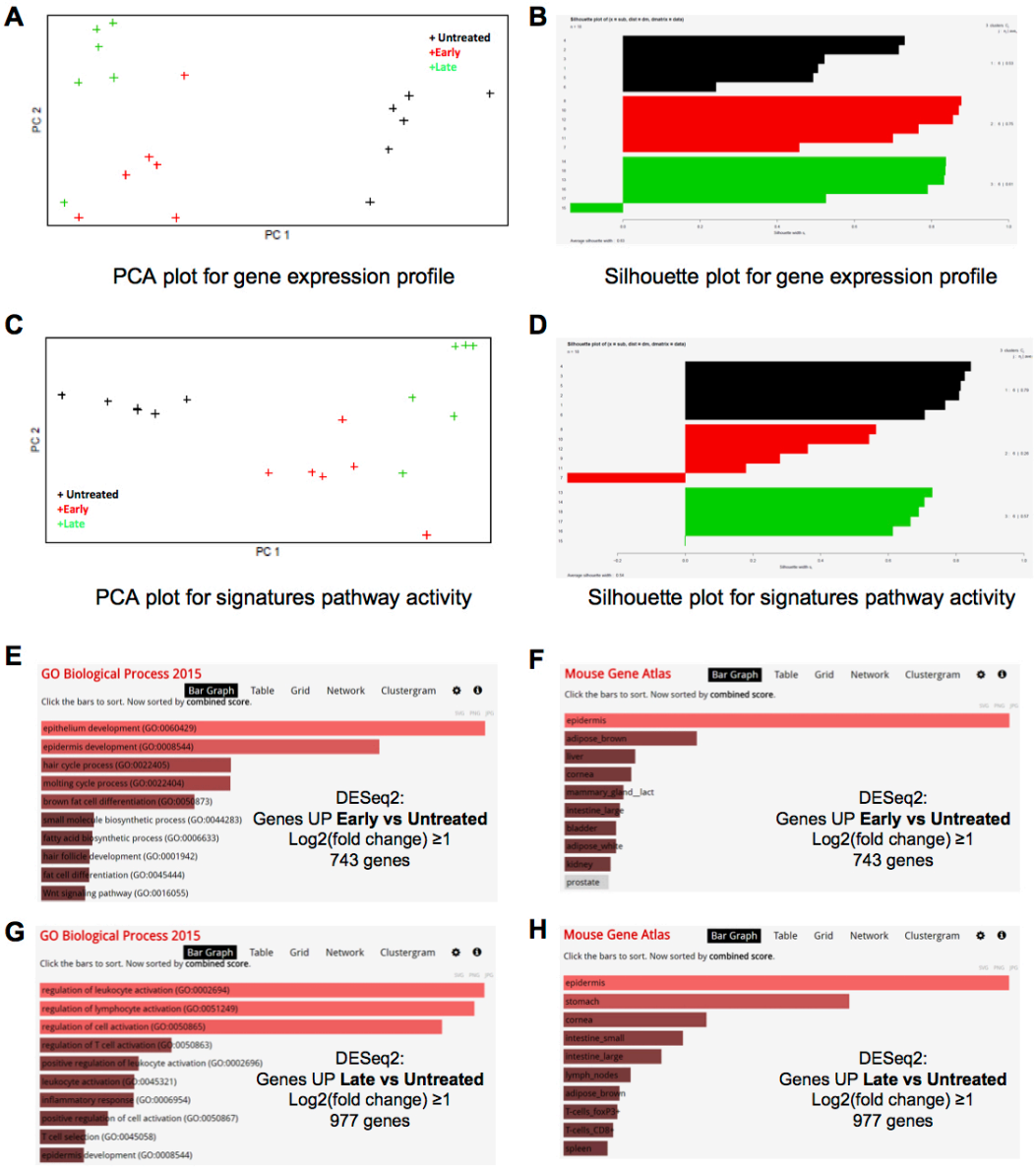

Figure 2.12. Classification of gene expression profile (A and B) and pathway activity signatures (C and D) using the principal component analysis (PCA) (A and C) and Silhouette Analysis (B and D) between untreated (black), 1 week MEKi (early, red) samples, and 12 weeks MEKi (late, green). (E-H) Up-regulated differentially expressed genes (cut-offs of $\log_2$FC ≥1 and p_{adj}≤0.05) determined by DESeq2 were used to query Enrichr for gene list enrichment analysis. The bar plots for GO Biological Process 2015 (E and G) and Mouse Gene Atlas (F and H) are shown for early (E and F) and late (G and H) time points on MEKi.

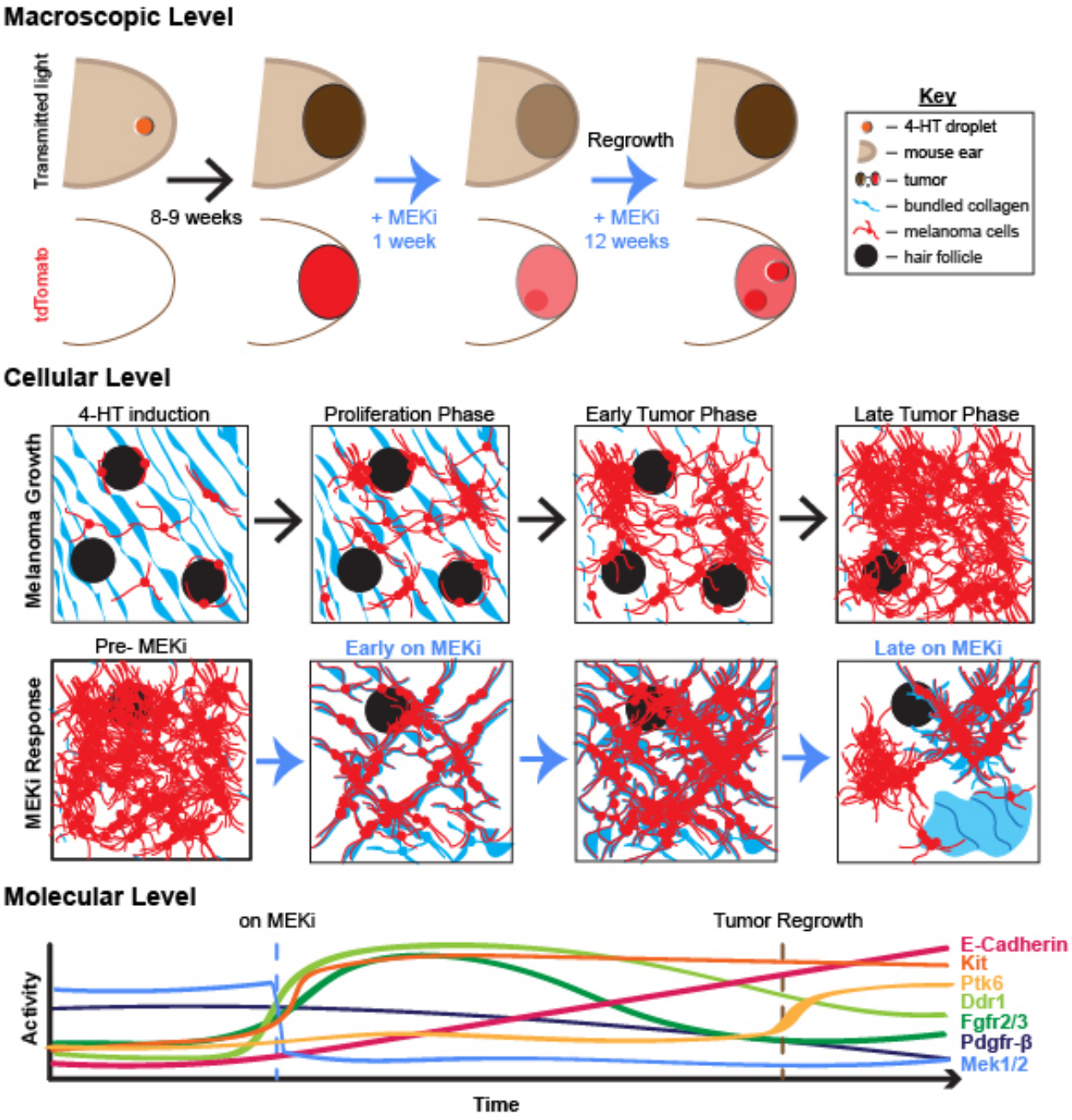

Figure 2.13. Graphical representation and model of results. Representation of tumor growth and response to MEKi at the macroscopic level, cellular and molecular levels. Representation of tdTomato+ melanoma and bundled collagen during tumor different phases of development and at early, intermediate, and late stages on MEKi. And illustrated diagram of key molecular hits that undergo plastic response over the course drug treatment. Graphic is based on intravital

imaging, MIB/MS, and mRNAseq of endogenous melanoma at different stages on treatment with MEKi.

CHAPTER 3: CONCLUDING THOUGHTS AND FUTURE DIRECTIONS

3.1 Overview

Through development of our model system and incorporation of intravital imaging strategies, I have made multiple observations that require further thought and investigation. Some of these are described below in further detail.

3.2 The extracellular matrix as a potential diagnostic of therapeutic resistance

Brief introduction and importance of the ECM in pathology

The extracellular matrix (ECM) is composed of approximately 300 proteins, known as the "matrisome" that assemble and rearrange in different patterns to generate the structural template for organs and tissues [79]. Structural deregulation within a tissue, which is mediated by changes of the ECM composition, can promote pathology, particularly in cancer and fibrotic disease [80]. In breast cancer, for example, tumor cells have been shown to migrate along collagen fiber tracks to promote invasion and metastasis [81,82]. And enhanced intratumoral tissue stiffness due to excess production of LOX (lysyl oxidase), which crosslinks collagen fibrils, is a common indicator of increased malignancy [83,84]. Additionally, deregulation of the ECM is thought to play a role in chronic wound settings, which are common in patients with diabetes, and treatment with fibronectin in chronic wounds has been shown to reduce disease state [85].

The bulk of the ECM is primarily composed of three different types of proteins: collagens, proteoglycans, and glycoproteins (Fig. 3.1). Collagens make up the structural component of the ECM important for tensile strength, and are present in both fibrillar (collagens I-III, V, and IX) and non-fibrillar forms. 43 known collagens are present in mammals, and they are one of the most highly expressed proteins in the body [86]. Proper regulation of collagen deposition and organization is critical during development, and loss of collagen elasticity due to

degradation over time is a promoting factor of aging [87]. Secondly, glycoproteins, such as fibronectin and laminins, bind to integrins and are critical for cell-ECM interactions. There are over 200 known glycoproteins, which can sequester soluble growth factors to further promote and inform migration and pro-survival cell signaling pathways. Interestingly, a recent and yet unpublished study from our lab by Dr. Seth Zimmerman shows that cells can generate and secrete their own fibronectin to promote directional migration. Furthermore, proteoglycans within the ECM can also bind soluble growth factor cues through interactions via their glycosaminoglycan (GAG) side chains. In both wound and tumor settings, the ECM is highly dynamic, and de-regulation of collagen crosslinking within the ECM has been shown to play a causative role in cancer pathogenesis [56].

Intravital imaging is now becoming a more popular tool to investigate tumor behavior in response to therapy, and as I demonstrated in chapter two, second harmonic generation can be an extraordinary tool used to directly visualize bundled collagen reorganization and behavior in situ. We have shown that on treatment with the selective MEK1/2 allosteric inhibitor, Trametinib, bundled collagen can be rearranged and enhanced over time during tumor persistence. These results suggest a significant role for collagen and the ECM in resistance to therapy. Recently, another study with the BRAF inhibitor, PLX-4720, also showed that drug treatment influenced the tumor microenvironment, and surviving tumor cells existed in regions with high stromal cell populations prior to acquiring genetic resistance [58]. These observations, made possible through intravital imaging techniques, illuminate the roles of the cellular and extracellular milieu within the tumor stroma in influencing innate and adaptive response to therapy. Since abnormal regulation of stomal ECM dynamics play a role in tumor progression, further longitudinal studies will be important in elucidating the interactions between tumor cells and the ECM during drug response to better characterize and inform therapeutic strategies.

Future directions: using ECM as a marker of drug resistance

Traditionally, it is taught that there exists only a very minute population of cancer cells with stem-like properties that may persist on drug to promote tumor recurrence. However, based on our intravital imaging studies, this model is incorrect (at least with targeted therapy). Instead, while there is a significant initial de-bulking of the tumor cell mass on MEKi, with tumor depth decreasing approximately 30% within the first week on drug, a substantial population of melanoma cells survive. Direct visualization of intratumoral response to MEKi in our studies suggest that there exists a strong structural component to therapeutic resistance, which may initially be independent of genetic expression, but may influence cellular phenotype over time. These ideas are graphically represented in Figure 3.2.

Understanding how targeted therapeutics affect the tumor microenvironment is critical for effectively treating melanoma. Tumor heterogeneity plays a substantial role in tumor resistance to targeted therapy. However, by performing intravital imaging of endogenous melanoma and bundled collagen in long-term longitudinal drug studies with MEKi, I discovered one common factor in persisting tumor cell populations. Based on our studies, surviving melanoma cells on MEKi co-localize with bundled collagen during initial stages on therapy. This suggests that tumor cell-ECM interactions along with increased deposition and concentration of collagen within a tumor may be a direct indicator of functional resistance to drug. With this in mind, early detection of enhanced bundled collagen presence may mark the “switching” point for when a tumor begins to regrow during the course of treatment. Below, I will outline several aims and future directions to further interrogate this idea.

Depending on the tumor type, degradation of collagen or enhanced stiffness of a tissue can be frequently used to assess tumor development, progression and malignant status. Our studies demonstrated that the tumor ECM may be critical in initial melanoma cell survival on MEKi, and although our experiments were performed in an endogenous setting within a relevant genetic model of melanoma; still, these studies were performed in mice. To further interrogate this potential mechanism of tumor cell persistence, and to make a difference in clinical settings,

we need to validate this observation in human melanoma samples. First, I aim to perform second harmonic generation microscopy of patient biopsy samples using the same (or a similar) intravital imaging modality. The goal in mind here is to assess the disease state during the course of a patient's treatment on a specific drug. Ideally, initial studies will incorporate tissue samples from patients on MEKi (Trametinib).

There exists a significant need for new and improved biomarkers of tumor resistance, as the time in which a tumor becomes resistant to a therapeutic is still a relative guessing game. If we can identify similar changes in second harmonic generation in patient samples compared to our murine studies, we can develop a system to provide a clear biomarker or diagnostic for when a melanoma is adapting to drug in early stages. This "read-out" can be used to inform medical professionals to provide better treatment strategies for potentially prolonging a patient's life.

For these studies, we will need to design a special platform or stage-insert for patient tissue samples (a "biopsy grip"), and we will need to develop better software analysis tools to generate a specific diagnostic measure of intratumoral bundled collagen concentration and organization with high resolution and certainty. Already with image analysis, we can identify the status of bundled collagen deposition and arrangement within melanoma samples through measuring the average intensity (which will measure density), and the alignment (measuring reorganization) of collagen within the tumor. With improved analysis, this screen could potentially provide a clear diagnostic, with more collagen organization and bundling suggesting a condition reminiscent of the early stage on drug, where persistent tumor cell populations exist but have not yet reprogrammed to promote tumor regrowth; and less organization suggesting a late response with functional resistance emerging. One caveat for these studies is that we will also need to obtain a non-tumor control from patients for comparison.

Finally, since histology played a key role in our results described in chapter 2, and since pathologists use traditional histology techniques and analysis to assess tumor status anyway,

we will to couple two-photon analysis with histological read outs. Ideally, we will use the same patient tissue sample for histology as we will use for our multiphoton imaging studies, so as to limit additional invasive procedures. Masson's trichrome staining in our murine melanoma model identified the ECM as a further potential diagnostic of tumor persistence, as collagen presence was significantly enhanced in late stages on MEKi compared to early stages and no drug control. Therefore, combining these two techniques to analyze the ECM within individual tissue samples will provide further resolution for the identification of drug response status.

If we accomplish these aims, my long-term goal will be to develop novel treatment strategies that incorporate this two-photon imaging regimen. If our finding holds true in human samples, and bundled collagen does in fact play a major role in therapeutic resistance, we can develop therapeutic regimes which include the use of ECM degrading enzymes. In fact, treatment with hyaluronidase, which degrades the ECM via catalyzing cleavage of hyaluronan (also upregulated in cancers), has previously been shown to enhance the efficacy of chemotherapy in melanoma and is regaining popularity [88]. To develop a new therapeutic strategy, these studies will again need to be performed in mice. The goal overall goal of this investigation will be to identify the point in which a tumor begins to "switch" into a resistant state on drug, treat with hyaluronidase (or similar enzyme), and determine whether we can prolong and improve the effects of existing therapeutics.

3.3 Broad future applications and ongoing studies

While I chose investigate response to targeted therapy in our *Tyr::CreER;BRAF^{CA};PTEN$^{lox/lox}$;tdTomato^{LSL}* melanoma GEM model for my main thesis project, this model can be used to characterize a multitude of 'black box' topics in melanoma research. Initially, I developed the precise 4-HT application method, controlling tumor growth in space and time, in order to generate a system that can be used to study the metastatic cascade. I was particularly interested in providing a platform that enabled tracking of endogenous tumor cell invasion, with the ability to readily identify distant colonization in vivo. This was made possible

through both my method of 4-HT application and the incorporation of the tdTomato fluorescent allele. One question that I failed to answer was: “what ‘phase’ of melanoma development at the two-photon level correlates with metastasis?” Our model, combined with intravital imaging, provides one of the first systems that can be used to serially track endogenous tumor growth from the individual cell stage. While pathologists can provide insight into how malignant a tumor is at a specific traditional ‘stage’ of melanoma growth (based on depth and radius), longitudinal studies need to be performed at the cell level to fully characterize the process of malignant cell transformation and invasion in situ.

Another huge black box in melanoma research pertaining to treatment strategies is: Do existing therapies inhibit or promote invasion and metastasis in vivo? While tumor shrinkage is a good indicator of successful response, metastasis is what ultimately kills people. Several problematic factors exist that limit our understanding and research of this question. For one, tumors in most murine models develop at different rates, and distinct treatment options in the clinic are available for different stages of melanoma progression (Table 1.1). Therefore, the answer to this question could rely on a number of variables, as one drug may be effective in blocking metastasis in one ‘stage’, but could fail in another.

Beyond interrogating the success of a therapy at different stages of tumor development to answer this question, we also need to ask, “what stage on drug?” Tumors are remarkably heterogeneous, and a therapeutic agent can affect specific regions within a tumor more reliably than others due to both extrinsic (e.g. avascular regions with strong stromal components) and intrinsic factors (e.g. tumor cell genetic predisposition). Additionally, melanoma becomes resistant to existing therapies, and most GEM models can only mimic early stages of drug response, due to high initial tumor burden. Our system provides a more holistic view of drug response, as it provides a platform for long-term longitudinal studies. However, this question remains: does targeted therapy also inhibit metastasis? Based on the results from our study with MEKi (Chapter 2), we can develop hypotheses for how MEKi influences tumor cell invasion

and metastasis at early and late stages on drug. For example, we identified an increase in E-Cadherin expression in late stages on MEKi. Recently, E-cadherin has been shown to be important for collective cell migration, which may play a critical role in disseminating from a primary tumor [33]. Furthermore, PI3K and AKT signatures were increased throughout drug treatment, which have been characterized in other drug studies modeling resistance. Notably, these pathways signal to Rac, which can promote and influence migration patterns and behaviors through signaling to the actin cytoskeleton. While these initial findings suggest that MEKi may actually promote malignancy in prolonged treatment settings, more conclusive studies need to be performed to directly interrogate and evaluate whether this is true for persistent melanoma populations in late stages on therapy.

3.5 Figures

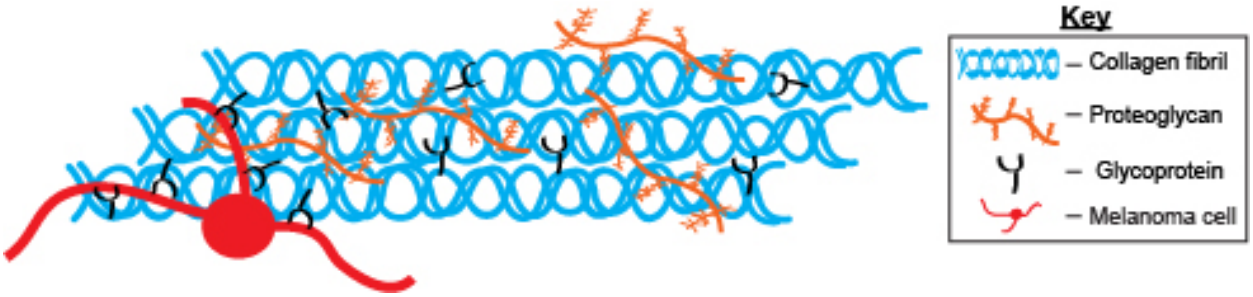

Figure 3.1 The extracellular matrix: three key components of the matrisome. Graphical representation of a melanoma cell interacting with collagens, proteoglycans, and glycoproteins in the ECM. Note: drawings not to scale.

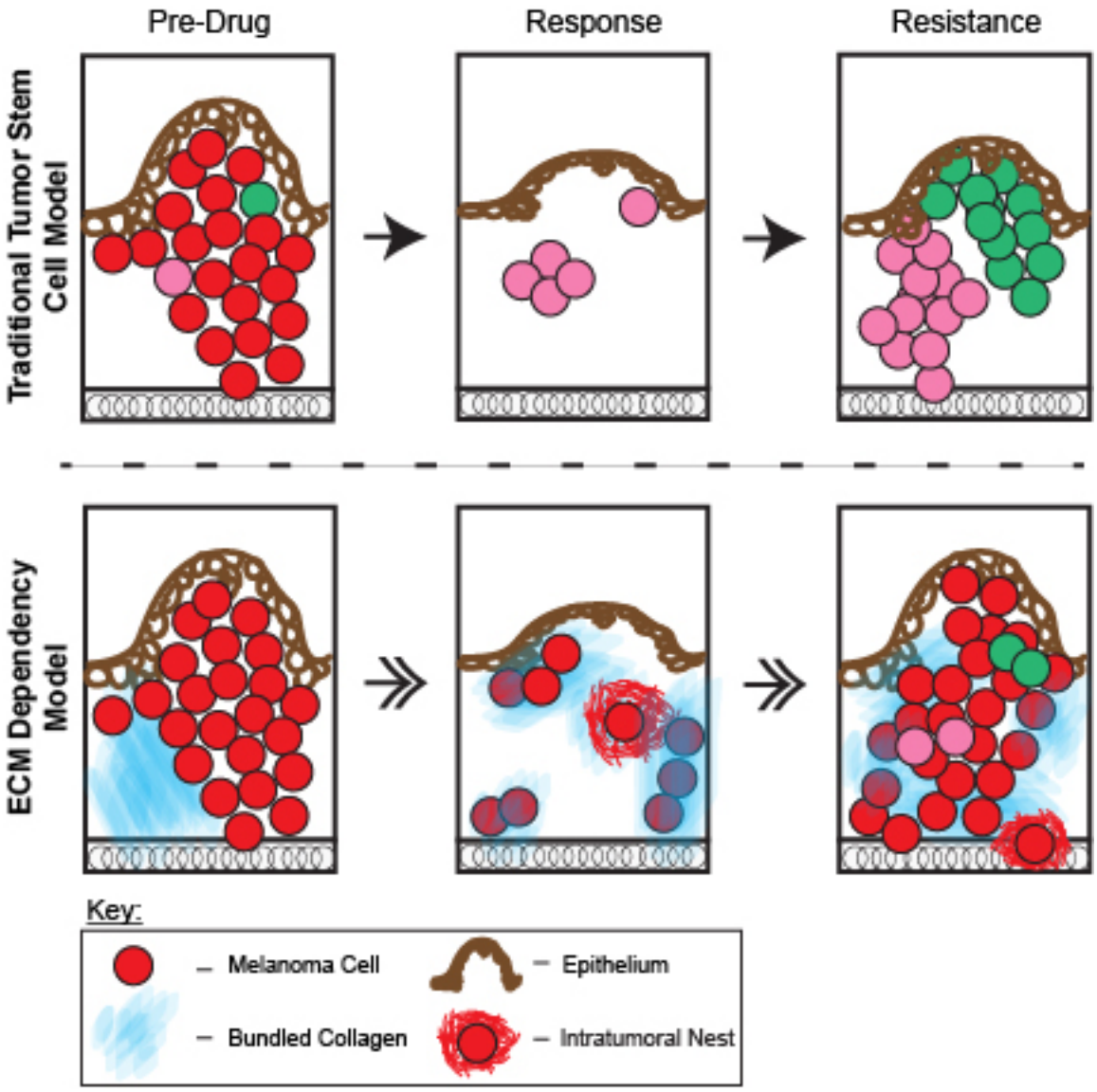

Figure 3.2 ECM dependency model for tumor cell persistence and functional resistance to drug. Traditional model of tumor response to therapy, where a pre-existing subset of tumor cells are genetically resistant to drug, compared to a new model, demonstrating structural dependency of bundled collagen for tumor cell persistence, followed by genetic expression changes in melanoma cell populations. Model not drawn to scale.

REFERENCES

1. Boyle, J. Molecular biology of the cell, 5th edition by B. Alberts, A. Johnson, J. Lewis, M. Raff, K. Roberts, and P. Walter. *Biochem. Mol. Biol. Educ.* **36,** 317–318 (2008).

2. Moshammer, H., Simic, S. & Haluza, D. UV-Radiation: From Physics to Impacts. *Int. J. Environ. Res. Public Health* **14,** 200 (2017).

3. Joselow, A., Lynn, D., Terzian, T. & Box, N. F. in *Methods in molecular biology (Clifton, N.J.)* **1534,** 175–184 (2017).

4. Sandru, A., Voinea, S., Panaitescu, E. & Blidaru, A. Survival rates of patients with metastatic malignant melanoma. *J. Med. Life* **7,** 572–6 (2014).

5. Ascierto, P. A. *et al.* The role of BRAF V600 mutation in melanoma. *J. Transl. Med.* **10,** 85 (2012).

6. Tran, N. H., Wu, X. & Frost, J. A. B-Raf and Raf-1 are regulated by distinct autoregulatory mechanisms. *J. Biol. Chem.* **280,** 16244–53 (2005).

7. Dankort, D. *et al.* Braf(V600E) cooperates with Pten loss to induce metastatic melanoma. *Nat. Genet.* **41,** 544–552 (2009).

8. Vredeveld, L. C. W. *et al.* Abrogation of BRAFV600E-induced senescence by PI3K pathway activation contributes to melanomagenesis. *Genes Dev.* **26,** 1055–1069 (2012).

9. Wong, S. Y. & Hynes, R. O. Lymphatic or hematogenous dissemination: how does a metastatic tumor cell decide? *Cell Cycle* **5,** 812–7 (2006).

10. Friedl, P. & Wolf, K. Tumour-cell invasion and migration: diversity and escape mechanisms. *Nat Rev Cancer* **3,** 362–374 (2003).

11. Leslie, M. Tumors have found a bloody new way to grow and spread. *Science (80-.).* (2016). doi:10.1126/science.aag0605

12. Friedl, P., Locker, J., Sahai, E. & Segall, J. E. Classifying collective cancer cell invasion. *Nat. Cell Biol.* **14,** 777–83 (2012).

13. Friedl, P. & Alexander, S. Cancer Invasion and the Microenvironment: Plasticity and Reciprocity. *Cell* **147,** 992–1009 (2017).

14. Balkwill, F. R., Capasso, M. & Hagemann, T. The tumor microenvironment at a glance. *J. Cell Sci.* **125,** 5591 LP-5596 (2013).

15. Kalal, B. S., Upadhya, D. & Pai, V. R. Chemotherapy resistance mechanisms in advanced skin cancer. *Oncol. Rev.* **11,** 326 (2017).

16. Agha, A. & Tarhini, A. A. Adjuvant Therapy for Melanoma. *Curr. Oncol. Rep.* **19,** 36 (2017).

17. Huang, A. C. *et al.* T-cell invigoration to tumour burden ratio associated with anti-PD-1

response. *Nature* (2017). doi:10.1038/nature22079

18. Wang, D. Y. *et al.* Clinical features of acquired resistance to anti-PD-1 therapy in advanced melanoma. *Cancer Immunol. Res.* canimm.0287.2016 (2017). doi:10.1158/2326-6066.CIR-16-0287

19. Nakasone, E. S. *et al.* Imaging Tumor-Stroma Interactions during Chemotherapy Reveals Contributions of the Microenvironment to Resistance. *Cancer Cell* **21,** 488–503 (2012).
20. Zitvogel, L., Pitt, J. M., Daillere, R., Smyth, M. J. & Kroemer, G. Mouse models in oncoimmunology. *Nat Rev Cancer* **16,** 759–773 (2016).

21. Tsien, R. Y. THE GREEN FLUORESCENT PROTEIN. *Annu. Rev. Biochem.* **67,** 509–544 (1998).

22. Combs, C. A. & Shroff, H. in *Current Protocols in Neuroscience* **79,** 2.1.1-2.1.25 (John Wiley & Sons, Inc., 2017).

23. Lippincott-Schwartz, J. Bridging Structure and Process in Developmental Biology through New Imaging Technologies. *Dev. Cell* **21,** 5–10 (2011).

24. Pittet, M. J. *et al.* Intravital imaging. *Cell* **147,** 983–91 (2011).

25. Svoboda, K. *et al.* Principles of two-photon excitation microscopy and its applications to neuroscience. *Neuron* **50,** 823–39 (2006).

26. Weigert, R., Sramkova, M., Parente, L. & Masedunskas, A. Intravital microscopy: a novel tool to study cell biology in living animals. *Histochem. Cell Biol.* **133,** 481–491 (2010).

27. Jenne, C. N., Wong, C. H. Y., Petri, B. & Kubes, P. The Use of Spinning-Disk Confocal Microscopy for the Intravital Analysis of Platelet Dynamics in Response to Systemic and Local Inflammation. *PLoS One* **6,** e25109 (2011).

28. Kedrin, D. *et al.* Intravital imaging of metastatic behavior through a Mammary Imaging Window. *Nat. Methods* **5,** 1019–1021 (2008).

29. Masedunskas, A. *et al.* Intravital microscopy: A practical guide on imaging intracellular structures in live animals. *Bioarchitecture* **2,** 143–157 (2012).

30. Isobe, K. *et al.* Background-free deep imaging by spatial overlap modulation nonlinear optical microscopy. *Biomed. Opt. Express* **3,** 1594–1608 (2012).

31. Yang, B. *et al.* Single-Cell Phenotyping within Transparent Intact Tissue through Whole-Body Clearing. *Cell* **158,** 945–958 (2014).

32. Chan, K. T. *et al.* Intravital imaging of a spheroid-based orthotopic model of melanoma in the mouse ear skin. *Intravital* **2,** e:25805 (2013).

33. Kai, M. P. *et al.* Tumor presence induces global immune changes and enhances nanoparticle clearance. *ACS Nano* **10,** (2016).

34. Roode, L. E. *et al.* Subtumoral analysis of PRINT nanoparticle distribution reveals

targeting variation based on cellular and particle properties. *Nanomedicine Nanotechnology, Biol. Med.* **12,** (2016).

35. Mohler, W., Millard, A. C. & Campagnola, P. J. Second harmonic generation imaging of endogenous structural proteins. *Methods* **29,** 97–109 (2003).

36. Mehnert, J. M. & Kluger, H. M. Driver Mutations in Melanoma: Lessons Learned From Bench-to-Bedside Studies. *Curr. Oncol. Rep.* **14,** 449–457 (2012).

37. Berger, M. F. *et al.* Melanoma genome sequencing reveals frequent PREX2 mutations. *Nature* **485,** 502–506 (2012).

38. Wan, P. T. C. *et al.* Mechanism of Activation of the RAF-ERK Signaling Pathway by Oncogenic Mutations of B-RAF. *Cell* **116,** 855–867 (2004).

39. T., F. K. *et al.* Improved Survival with MEK Inhibition in BRAF-Mutated Melanoma. *N. Engl. J. Med.* **367,** 107–114 (2012).

40. V., L. G. *et al.* Combined BRAF and MEK Inhibition versus BRAF Inhibition Alone in Melanoma. *N. Engl. J. Med.* **371,** 1877–1888 (2014).

41. Wellbrock, C. & Arozarena, I. The Complexity of the ERK/MAP-Kinase Pathway and the Treatment of Melanoma Skin Cancer. *Front. Cell Dev. Biol.* **4,** 33 (2016).

42. Karimkhani, C., Gonzalez, R. & Dellavalle, R. P. A Review of Novel Therapies for Melanoma. *Am. J. Clin. Dermatol.* **15,** 323–337 (2014).

43. Long, G. V *et al.* Dabrafenib and trametinib versus dabrafenib and placebo for Val600 BRAF-mutant melanoma: a multicentre, double-blind, phase 3 randomised controlled trial. *Lancet* **386,** 444–451 (2017).

44. Perna, D. *et al.* BRAF inhibitor resistance mediated by the AKT pathway in an oncogenic BRAF mouse melanoma model. *Proc. Natl. Acad. Sci. U. S. A.* **112,** E536-45 (2015).

45. Spagnolo, F., Ghiorzo, P. & Queirolo, P. Overcoming resistance to BRAF inhibition in BRAF-mutated metastatic melanoma. *Oncotarget* **5,** 10206–21 (2014).

46. Manzano, J. L. *et al.* Resistant mechanisms to BRAF inhibitors in melanoma. *Ann. Transl. Med.* **4,** 237 (2016).

47. Usary, J. *et al.* Predicting Drug Responsiveness in Human Cancers Using Genetically Engineered Mice. *Clin. Cancer Res.* **19,** 4889 LP-4899 (2013).

48. Hoek, K. S. *et al.* In vivo Switching of Human Melanoma Cells between Proliferative and Invasive States. *Cancer Res.* **68,** 650 LP-656 (2008).

49. Kemper, K., de Goeje, P. L., Peeper, D. S. & van Amerongen, R. Phenotype Switching: Tumor Cell Plasticity as a Resistance Mechanism and Target for Therapy. *Cancer Res.* **74,** 5937 LP-5941 (2014).

50. Sanchez-Laorden, B. *et al.* BRAF Inhibitors Induce Metastasis in RAS Mutant or Inhibitor-

Resistant Melanoma Cells by Reactivating MEK and ERK Signaling. *Sci. Signal.* **7,** ra30 LP-ra30 (2014).

51. Roesch, A. Tumor heterogeneity and plasticity as elusive drivers for resistance to MAPK pathway inhibition in melanoma. *Oncogene* **34,** 2951–2957 (2015).

52. Straussman, R. *et al.* Tumour micro-environment elicits innate resistance to RAF inhibitors through HGF secretion. *Nature* **487,** 500–504 (2012).

53. Smith, M. P. *et al.* The Immune Microenvironment Confers Resistance to MAPK Pathway Inhibitors through Macrophage-Derived TNFα. *Cancer Discov.* **4,** 1214 LP-1229 (2014).

54. Menzies, A. M. *et al.* Inter- and Intra-Patient Heterogeneity of Response and Progression to Targeted Therapy in Metastatic Melanoma. *PLoS One* **9,** 1–9 (2014).

55. Egeblad, M., Nakasone, E. S. & Werb, Z. Tumors as Organs: Complex Tissues that Interface with the Entire Organism. *Dev. Cell* **18,** 884–901 (2017).

56. Hofschröer, V. *et al.* Extracellular protonation modulates cell-cell interaction mechanics and tissue invasion in human melanoma cells. *Sci. Rep.* **7,** 42369 (2017).

57. Sandri, S. *et al.* Vemurafenib resistance increases melanoma invasiveness and modulates the tumor microenvironment by MMP-2 upregulation. *Pharmacol. Res.* **111,** 523–533 (2016).

58. Hirata, E. *et al.* Intravital Imaging Reveals How BRAF Inhibition Generates Drug-Tolerant Microenvironments with High Integrin β1/FAK Signaling. *Cancer Cell* **27,** 574–588 (2015).

59. Cox, T. R. & Erler, J. T. Remodeling and homeostasis of the extracellular matrix: implications for fibrotic diseases and cancer. *Dis. Model. & Mech.* **4,** 165 LP-178 (2011).

60. Madisen, L. *et al.* A robust and high-throughput Cre reporting and characterization system for the whole mouse brain. *Nat. Neurosci.* **13,** 133–140 (2010).

61. Das Thakur, M., Pryer, N. K. & Singh, M. Mouse tumour models to guide drug development and identify resistance mechanisms. *J. Pathol.* **232,** 103–111 (2014).

62. ROTHSTEIN, E. C., NAUMAN, M., CHESNICK, S. & BALABAN, R. S. Multi-photon excitation microscopy in intact animals. *J. Microsc.* **222,** 58–64 (2006).

63. Hanahan, D. & Weinberg, R. A. Hallmarks of cancer: The next generation. *Cell* **144,** 646–674 (2011).

64. Zawistowski, J. S. *et al.* MicroRNA 9-3p targets beta1 integrin to sensitize claudin-low breast cancer cells to MEK inhibition. *Mol. Cell. Biol.* **33,** 2260–2274 (2013).

65. Tschandl, P. *et al.* Impact of oncogenic BRAF mutations and p16 expression on the growth rate of early melanomas and naevi *in vivo*. *Br. J. Dermatol.* **174,** 364–370 (2016).

66. Lu, P., Weaver, V. M. & Werb, Z. The extracellular matrix: A dynamic niche in cancer

progression. *J. Cell Biol.* **196,** 395–406 (2012).

67. Shi, H. *et al.* Acquired Resistance and Clonal Evolution in Melanoma during BRAF Inhibitor Therapy. *Cancer Discov.* **4,** 80 LP-93 (2014).

68. Obenauf, A. C. *et al.* Therapy-induced tumour secretomes promote resistance and tumour progression. *Nature* **520,** 368–372 (2015).

69. Hugo, W. *et al.* Non-genomic and Immune Evolution of Melanoma Acquiring MAPKi Resistance. *Cell* **162,** 1271–1285 (2015).

70. Duncan, J. S. *et al.* Dynamic Reprogramming of the Kinome in Response to Targeted MEK Inhibition in Triple-Negative Breast Cancer. *Cell* **149,** 307–321 (2012).

71. Stuhlmiller, T. J. *et al.* Inhibition of Lapatinib-Induced Kinome Reprogramming in ERBB2-Positive Breast Cancer by Targeting BET Family Bromodomains. *Cell Rep.* **11,** 390–404 (2015).

72. Love, M. I., Huber, W. & Anders, S. Moderated estimation of fold change and dispersion for RNA-seq data with DESeq2. *Genome Biol.* **15,** 550 (2014).

73. Gatza, M. L., Silva, G. O., Parker, J. S., Fan, C. & Perou, C. M. An integrated genomics approach identifies drivers of proliferation in luminal-subtype human breast cancer. *Nat Genet* **46,** 1051–1059 (2014).

74. Weina, K. *et al.* TGF- *β* induces SOX2 expression in a time-dependent manner in human melanoma cells. *Pigment Cell Melanoma Res.* **29,** 453–458 (2016).

75. Harris, M. L., Baxter, L. L., Loftus, S. K. & Pavan, W. J. Sox proteins in melanocyte development and melanoma. *Pigment Cell Melanoma Res.* **23,** 496–513 (2010).

76. Cieply, B., Farris, J., Denvir, J., Ford, H. L. & Frisch, S. M. Epithelial–Mesenchymal Transition and Tumor Suppression Are Controlled by a Reciprocal Feedback Loop between ZEB1 and Grainyhead-like-2. *Cancer Res.* **73,** 6299 LP-6309 (2013).

77. Werner, S. *et al.* Dual Roles of the Transcription Factor Grainyhead-like 2 (GRHL2) in Breast Cancer. J Biol Chem. **32**, 22993-3008 (2013).

78. Chen, E. Y. *et al.* Enrichr: interactive and collaborative HTML5 gene list enrichment analysis tool. *BMC Bioinformatics* **14,** 128 (2013).

79. Bonnans, C., Chou, J. & Werb, Z. Remodelling the extracellular matrix in development and disease. *Nat Rev Mol Cell Biol* **15,** 786–801 (2014).

80. Fang, M., Yuan, J., Peng, C. & Li, Y. Collagen as a double-edged sword in tumor progression. *Tumor Biol.* **35,** 2871–2882 (2014).

81. Clark, A. G. & Vignjevic, D. M. Modes of cancer cell invasion and the role of the microenvironment. *Curr. Opin. Cell Biol.* **36,** 13–22 (2015).

82. Nelson, M. T. *et al.* Preferential, enhanced breast cancer cell migration on biomimetic

electrospun nanofiber `cell highways'. *BMC Cancer* **14,** 825 (2014).

83. ZHANG, Q. *et al.* Upregulated expression of LOX is a novel independent prognostic marker of worse outcome in gastric cancer patients after curative surgery. *Oncol. Lett.* **5,** 896–902 (2013).

84. Villanueva, M. T. Metastasis: LOX does some prepping. *Nat Rev Cancer* **15,** 384–385 (2015).

85. Moroz, A. *et al.* Platelet-rich plasma and chronic wounds: remaining fibronectin may influence matrix remodeling and regeneration success. *Cytotherapy* **15,** 1436–9 (2013).

86. Brinckmann, J. Collagens at a glance. *Top. Curr. Chem.* **247,** 1–6 (2005).

87. Stearns-Reider, K. M. *et al.* Aging of the skeletal muscle extracellular matrix drives a stem cell fibrogenic conversion. *Aging Cell* **16**, 518-528 (2017).

88. Whatcott, C. J., Han, H., Posner, R. G., Hostetter, G. & Von Hoff M, D. Targeting the tumor microenvironment in cancer: why hyaluronidase deserves a second look. *Cancer Discov.* **1,** 291–296 (2011).